

THE VARIANCE OF METHANE ADSORPTION AND
ITS RELATION TO THERMAL MATURITY
IN THE MARCELLUS SHALE

by

ALEXANDER ADDISON MILLER

Presented to the Faculty of the Graduate School of
The University of Texas at Arlington in Partial Fulfillment
of the Requirements
for the Degree of

MASTER OF SCIENCE IN GEOLOGY

THE UNIVERSITY OF TEXAS AT ARLINGTON

DECEMBER 2015

Copyright © by Alexander Miller 2015

All Rights Reserved



Acknowledgements

I would like to thank Martin Emery and Range Resources for making this project possible. Martin, thank you for your guidance along every step of this project and for the funding of much needed additional data. Thank you Dr. Wickham for mentoring me through my graduate student career, and for your guidance and input with this project. I'd like to thank my committee members Dr. Qinhong Hu and Dr. Majie Fan for their guidance and input on this project as well as my graduate career. I'd also like to thank the Laboratory and industry participants in this project that enabled me the use of their data. Without this comprehensive data set the project doesn't exist.

Thank you to my parents Tim and Helen Miller for financially and emotionally supporting me through my undergraduate and graduate schooling. They understood the importance of furthering my education and helped to make it happen. And finally, thank you Jena Tuite for all of your support and moving to Texas with me to pursue this degree and further my career.

October 26, 2015

Abstract

THE VARIANCE OF METHANE ADSORPTION AND
ITS RELATION TO THERMAL MATURITY
IN THE MARCELLUS SHALE

Alexander Miller, MS

The University of Texas at Arlington, 2015

Supervising Professor: John Wickham

In unconventional shale gas plays, gas-in-place is a major factor in evaluating the shale's potential and determining well density and lateral placement. The two main contributors to total gas-in-place are free gas and adsorbed gas. Gas in pores, "free" gas and adsorbed gas, which equal gas-in-place when summed, contribute to production from unconventional mudstone reservoirs like the Middle Devonian Marcellus Shale in the Appalachian Basin. Gas-in-place and production volumes however, vary throughout the different areas of Marcellus production in the basin. This paper analyzes the change in volumes of adsorbed methane through the geologically different regions of Marcellus production. Comparing samples from the main production areas, two results are evident. The first is that Langmuir methane adsorption storage capacity (G_{SL} , scf/ton) varies primarily with TOC and thermal maturity. The second observation is that other factors influence G_{SL} such as porosity, bulk density, clay content, and resistivity. Through multiple regression analysis, a model was created to predict G_{SL} from its most significant factors.

Table of Contents

Acknowledgements	iii
Abstract.....	iv
List of Illustrations	vi
List of Tables	viii
Chapter 1 Introduction	1
Chapter 2 Geologic Setting	3
Appalachian Basin Geologic History.....	3
Regional Stratigraphy	5
Members of the Marcellus.....	6
Chapter 3 Previous Studies.....	10
Chapter 4 Data Set.....	11
Chapter 5 Methods	17
Methane Adsorption Isotherm.....	17
Thermal Maturity	21
Programmed Pyrolysis	21
Vitrinite Reflectance.....	27
X-Ray Diffraction.....	28
Multiple Regression Analysis.....	28
Spotfire Analytics	29
Chapter 6 Results.....	30
Chapter 7 Discussion and Interpretation	46
Chapter 8 Conclusions	62
References	64
Biographical Information.....	67

List of Illustrations

Figure 1-1 Gas produced (scf/ton) vs. Pressure (psia)	2
Figure 2-1 Paleogeographic map of the Middle Devonian (385 ma).....	4
Figure 2-2 Unconventional Wells Drilled in Pennsylvania	6
Figure 2-3 Type logs of Marcellus Formation from core production areas.....	8
Figure 4-1 Map of study area with numbered data points	11
Figure 5-1 Generalized setup for adsorption isotherm testing	20
Figure 5-2 Type logs of Marcellus Formation from core production areas.....	22
Figure 5-3 Programmed Pyrolysis responses	23
Figure 5-4 TOC vol% vs. TOC wt%.....	25
Figure 5-5 Pseudo Van Krevlin diagram highlighting maturity trends	26
Figure 5-6 Pseudo Van Krevlin diagram for data set	27
Figure 6-1 G_{SL} , Langmuir Storage Capacity (scf/ton) vs. Sample Number	32
Figure 6-2 Thermal Maturity (V_{ROE}) vs. Sample Number	33
Figure 6-3 TOC vol% vs. Sample number.....	34
Figure 6-4 Clay vol% vs. Sample Number	35
Figure 6-5 Porosity % vs. Sample Number	36
Figure 6-6 G_{SL} , Langmuir Storage Capacity (scf/ton) vs. TOC vol%.....	37
Figure 6-7 Normalized G_{SL} / TOC (scf/(ton*toc vol%)) vs. Thermal Maturity (V_{ROE})	38
Figure 6-8 Porosity % vs. Thermal Maturity (V_{ROE})	39
Figure 6-9 P_L , Langmuir Pressure (psia) vs. Thermal Maturity (V_{ROE})	40
Figure 6-10 Thermal Maturity (V_{ROE}) vs. Deep Resistivity (ohm*m).....	41
Figure 6-11 G_{SL} , Langmuir Storage Capacity (scf/ton) vs. Clay vol%.....	42
Figure 6-12 G_{SL} , Langmuir Storage Capacity (scf/ton) vs. Porosity %.....	43
Figure 6-13 Bulk Density (g/cc) vs. Porosity %	44
Figure 6-14 Bulk Density (g/cc) vs. Thermal Maturity (V_{ROE})	45

Figure 7-1 G_{SL} , Langmuir Storage Capacity (scf/ton) vs. G_{SLM} , Modeled Langmuir Storage Capacity (scf/ton).....	53
Figure 7-2 Uranium (ppm) vs. Gamma Ray (API)	54
Figure 7-3 TOC vol% vs. TOC_M , Modeled TOC vol% from U and Bulk Density	57
Figure 7-4 G_{SL} , Langmuir Storage Capacity (scf/ton) vs. G_{SLM} Modeled Langmuir Storage Capacity with TOC_M (scf/ton).....	59
Figure 7-5 Type logs of Marcellus Formation from core production areas with TOC_M and G_{SLM} curves plotted	61

List of Tables

Table 4-1 Sample Number, Region, Well Code, Elevation, Sample Depth, Subsea Depth, Formation Member, Depositional Setting, Isotherm Temperature, G_S In-Situ Storage Capacity, P Reservoir Pressure, G_{SL} Langmuir Storage Capacity, P_L Langmuir Pressure	12
Table 4-2 Normalized adsorption capacities (in-situ and Langmuir) by vol% and wt% TOC, TOC vol%, TOC wt%, G_{SLM} , TOC_M , G_{SLM} with TOC_M	13
Table 4-3 Pyrolysis results, Thermal maturity (V_{ROE}) whole well & by formation member, Deep resistivity (ohm*m), Uranium (ppm), Gamma Ray (API)	14
Table 4-4 Mineralogies from XRD in wt%	15
Table 4-5 Mineralogies from XRD in vol%, Porosity %, Bulk Density (g/cc)	16
Table 7-1 Multiple Regression Analysis statistics from G_{SLM}	51
Table 7-2 Multiple Regression Analysis statistics from TOC_M	55
Table 7-3 Multiple Regression Analysis statistics from G_{SLM} using all logs	58

Chapter 1

Introduction

As of September 2015, the Marcellus Shale is producing approximately 16.4 bcf/day, and accounts for 36% of American shale gas production, making the Marcellus the largest unconventional shale gas play in the United States (US EIA, 2015). As production grows and geologists explore beyond sweet spots, gas-in-place serves as an important factor in directing capital expenses for drilling. Gas-in-place is comprised of free gas and sorbed gas (Ambrose et al., 2010). Adsorption is an important factor of gas in place, and according to Lu et al. (1995), and Schettler et al. (1991), adsorbed gas accounts for 61% and roughly 50%, respectively, of total gas in Devonian shales. Figure 1-1 is a graph from Heller and Zoback (2014) that shows a production model of gases produced as pressure declines from a Marcellus sample. As pressure decreases the volume produced of free gas and adsorbed gas both increase. Heller and Zoback (2014) suggest that desorption of methane is partly responsible for flat production decline curves.

To date, there is no published study quantifying the adsorptive storage capacity of the Marcellus Formation. Many other studies have published the properties of methane adsorption in shales, but none with the focus solely on the Marcellus. Gasparik et al. (2012) and Lu et al. (1995) both tested the adsorption of specific clays and while there was adsorbed methane on clays, it was minimal compared to the overall capacity of an organic shale. Furthermore, no relationships could be established between total clay content and adsorptive storage capacity. All of the mentioned studies found a positive linear correlation between total organic carbon weight percent (TOC wt%) and adsorptive storage capacity. Furthermore, it was found that adsorptive storage capacity for methane increased with increasing thermal maturity. Zhang et al. (2013) and Gasparik et al. (2012) both observed a change in this trend when samples of highest thermal maturities had lower adsorptive storage capacities than lower maturity samples. Levels of thermal maturity where storage capacity began to decrease varied in these studies, but both studies found that storage capacity decreased when vitrinite reflectance equivalent (V_{ROE}) was greater

than 2%. This paper compares the maximum (Langmuir) adsorptive storage capacities for a Marcellus Formation data set with TOC volume percent (TOC vol%), mineralogy, and thermal maturity.

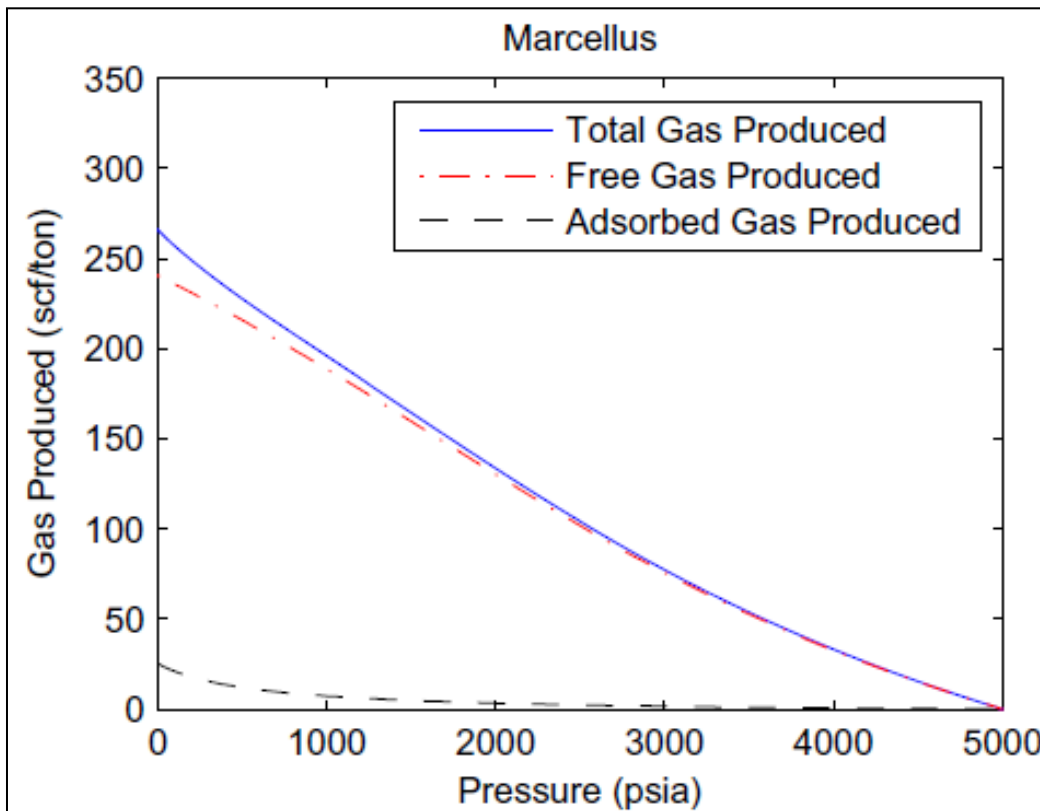


Figure 1-1 Gas produced (scf/ton) vs. Pressure (psia)

From Heller and Zoback (2014). Modeled Marcellus gas production vs. pressure. As pressure decreases adsorbed gas volume produced increases. Figure volumes not indicative of all Marcellus shale wells.

Chapter 2

Geologic Setting

Appalachian Basin Geologic History

The geologic history of the Appalachian basin began in the Neoproterozoic era of the Precambrian. Continent separation along the east coast of today's United States created many rifts along the eastern North American continent, Laurentia. Due to this continent separation, the Rome trough developed as a rift through western and central Pennsylvania (Faill, 1999). By the end of Precambrian time, an uplift to the east of the Rome trough provided clastic material that had begun to fill the trough. At the beginning of the Cambrian, the entire east coast became a passive continental margin with continued continent separation. A westward transgression resulted in multiple carbonate deposits in the Appalachian basin lasting through the middle Ordovician.

A reversal of the continent separation that created the Rome trough initiated the beginning of the Taconic Orogeny during the middle Ordovician. Oceanic crust was subducted under a volcanic arc micro continent as convergence began and the micro continent moved westward to the Laurentian continental shelf. Further convergence initiated multiple thrust faults that formed a tectonic wedge creating the Taconic Mountains in today's easternmost Pennsylvania. As the mountains rose, the Appalachian basin began to fill to the west with sands shales and conglomerates (Faill, 1999; Olusanmi et al., 2013).

The Acadian Orogeny began in the early Devonian and can be marked regionally by what is called the Tioga Ash bed (Faill, 1999). The collision of another volcanic micro continent with Laurentia, followed by collisional thrusting is responsible for the mountain building of this episode (Park et al., 2010). Following deposition of the Tioga Ash bed the Marcellus Formation was deposited, accompanied by rapid subsidence. Figure 2-1 is a paleogeographic map modified from Blakey showing the paleogeographic setting of the Appalachian Basin in the Middle Devonian (2013). As clastic sedimentation decreased, the Tully Limestone was deposited over a widespread area. Upper Devonian through middle Pennsylvanian time is represented by an influx

of sediment in the form of westward prograding deltas. Middle Pennsylvanian through Permian time is represented by widespread swamp environments that produced coal.

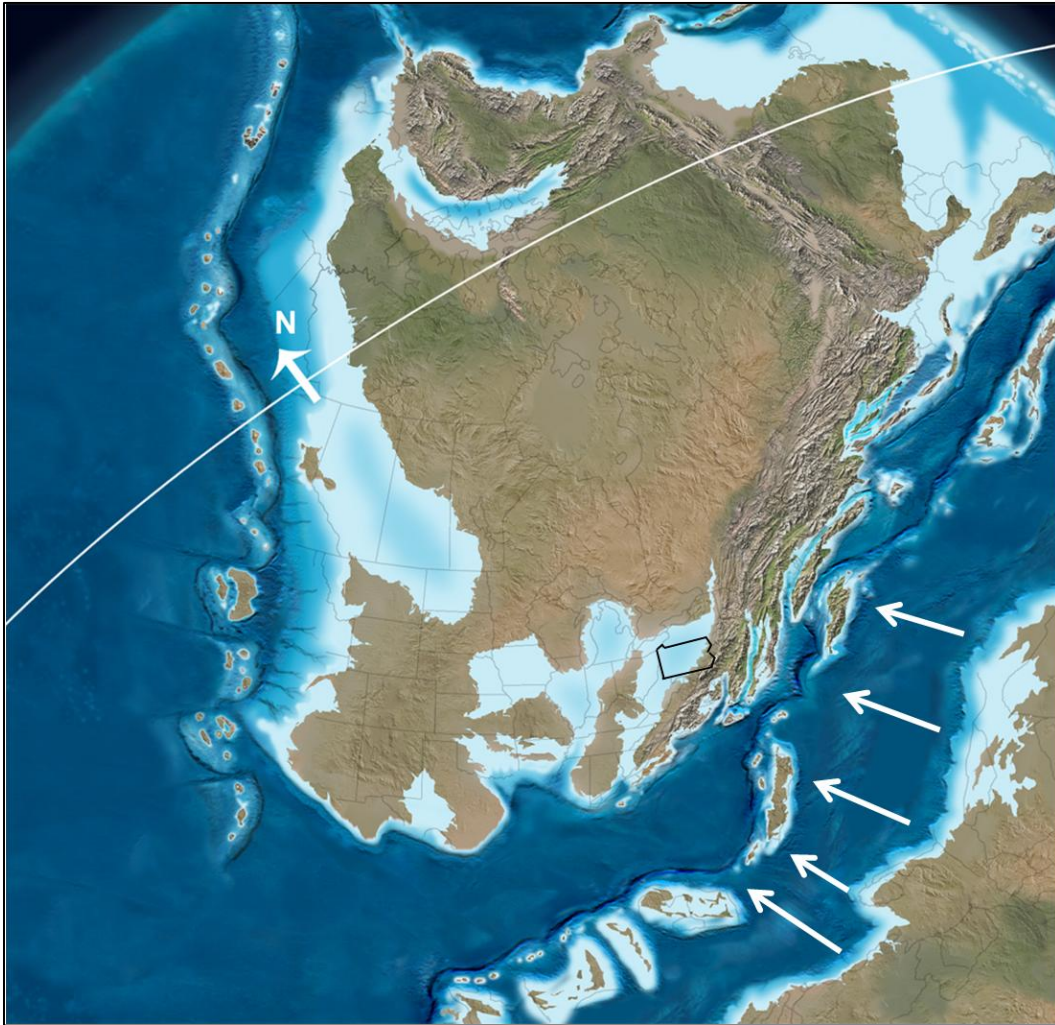


Figure 2-1 Paleogeographic map of the Middle Devonian (385 ma)

Modified from Blakey (2013). State of Pennsylvania outlined in black. White arrows indicate movement of island arc and African continent towards Laurentian continent.

The final major orogeny is the Allegheny Orogeny. This orogeny originated from the continent-to-continent collision of the Laurentian (North American) and African Plates, beginning from early Pennsylvanian to early Permian, depending on the author (Faill, 1999; Kulander and Ryder, 2005). This collision began with a series of low angle basement rooted thrust faults dipping to the south east. As the faults propagated to the northwest, the more ductile Paleozoic rocks kink folded above terminating thrust fault planes. The final product of this collision resulted in a relatively undeformed Appalachian plateau in western Pennsylvania, a valley and ridge province of parallel fold and thrust faults in the foreland of the Appalachian basin, and a complex southeastern area consisting of overlapping thrust sheets (Faill, 1999; Ruppert and Ryder, 2014).

Regional Stratigraphy

For the purposes of this study, the Marcellus Formation producing area is divided into two regions in southwest and northeast Pennsylvania. These regions were chosen because they are considered the areas of highest production in the play (Figure 2-2, MCOR, 2015). Figure 2-3 contains type logs for the Marcellus Formation from southwest and northeast PA. The southwest type log, located in Washington County, is west of the depocenter of the basin and was deposited in a shelf like environment (Olusanmi, 2013). From the southwest area, moving deeper into the basin from west to east, the Marcellus Formation thickens. The type log for the northeast area is located in Lycoming County and shows a thicker Marcellus section than the southwest area (Figure 2-3). This thickness increase on this type log is attributed to its proximity to the depositional foredeep of the basin. In the foredeep, sedimentation and subsidence rates are higher than any other parts of the basin (Decelles and Giles, 1996; Olusanmi, 2013). Track 1 on the type log contains a caliper and gamma ray API with red shading of values greater than 200 API. Track 2 contains resistivity, red being shallow and green being deep. Track 3 contains bulk density in black, density porosity in blue, neutron porosity in dashed red, and density correction in fine black.

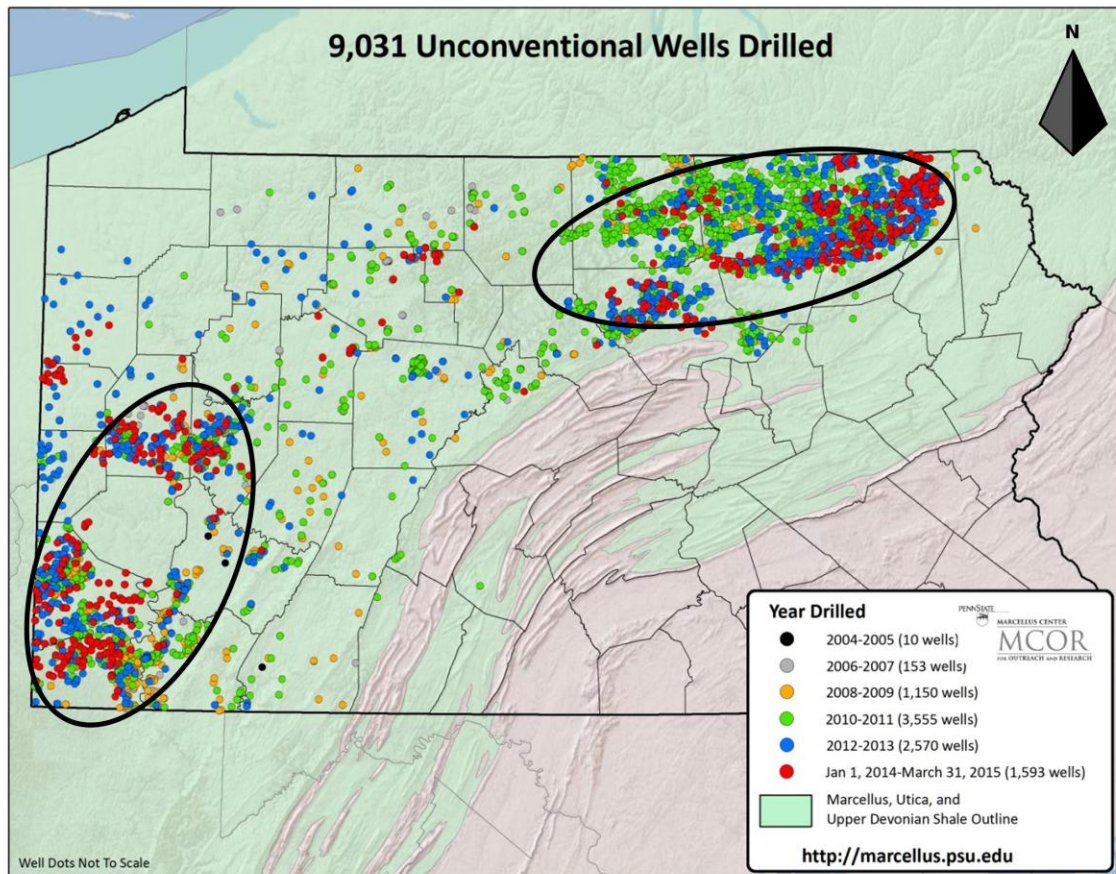


Figure 2-2 Unconventional Wells Drilled in Pennsylvania

Map of Pennsylvania indicating two main regions where unconventional wells in Pennsylvania have been drilled to date (Marcellus Center for Outreach and Research, <http://marcellus.psu.edu>)

Members of the Marcellus

For this thesis, certain comparisons are highlighted by formation member and depositional setting. Formation Members are Union Springs shale, Cherry Valley Limestone, and Oatka Creek shale (Figure 2-3) (Lash and Engelder, 2009). The Union Springs member is the oldest member of the Marcellus Formation and directly overlies the Onondaga Limestone. In the northeast part of the study area (Figure 2-3) the Union Springs has two different sections, a lower section with gamma ray (GR) API values greater than 200 API, and an upper section with lower GR API values. In the southwest part of the study area, this section is condensed and only

consists of an elevated GR API section. The lower Union Springs is characterized on a wireline log by the highest GR API units in the entire Marcellus Formation (200 to 600 API), the highest resistivities, and the lowest bulk densities. This interval has the highest TOC content (up to 20 vol % in the data set) and low clay content. Pyrite and algal cysts are both abundant.

In the northeast, the upper Union Springs' GR API's average is 150 API. Resistivities are lower and bulk densities are higher than the lower, higher GR API interval. The upper Union Springs commonly has higher clay content than the lower section, a lower TOC (6-13 vol %), has high pyrite content, and contains few burrows. The Union Springs member is capped by the Cherry Valley Limestone.

The Oatka Creek Member is the youngest member of the Marcellus Formation. Residing above the Cherry Valley Limestone, this member contains a lower amount of organics but still contains a significant amount of gas-in-place. Gamma ray values vary for this member due to a changing sequence of depositional settings. In this member, resistivity's decrease, bulk density increases, and some bioturbation can be observed. The lower organic content of this member can be attributed to a larger clastic influence, diluting the organic concentration. Overlying the Marcellus is the Mahantango Formation, a non-organic grey shale, which is capped by the Tully Limestone.

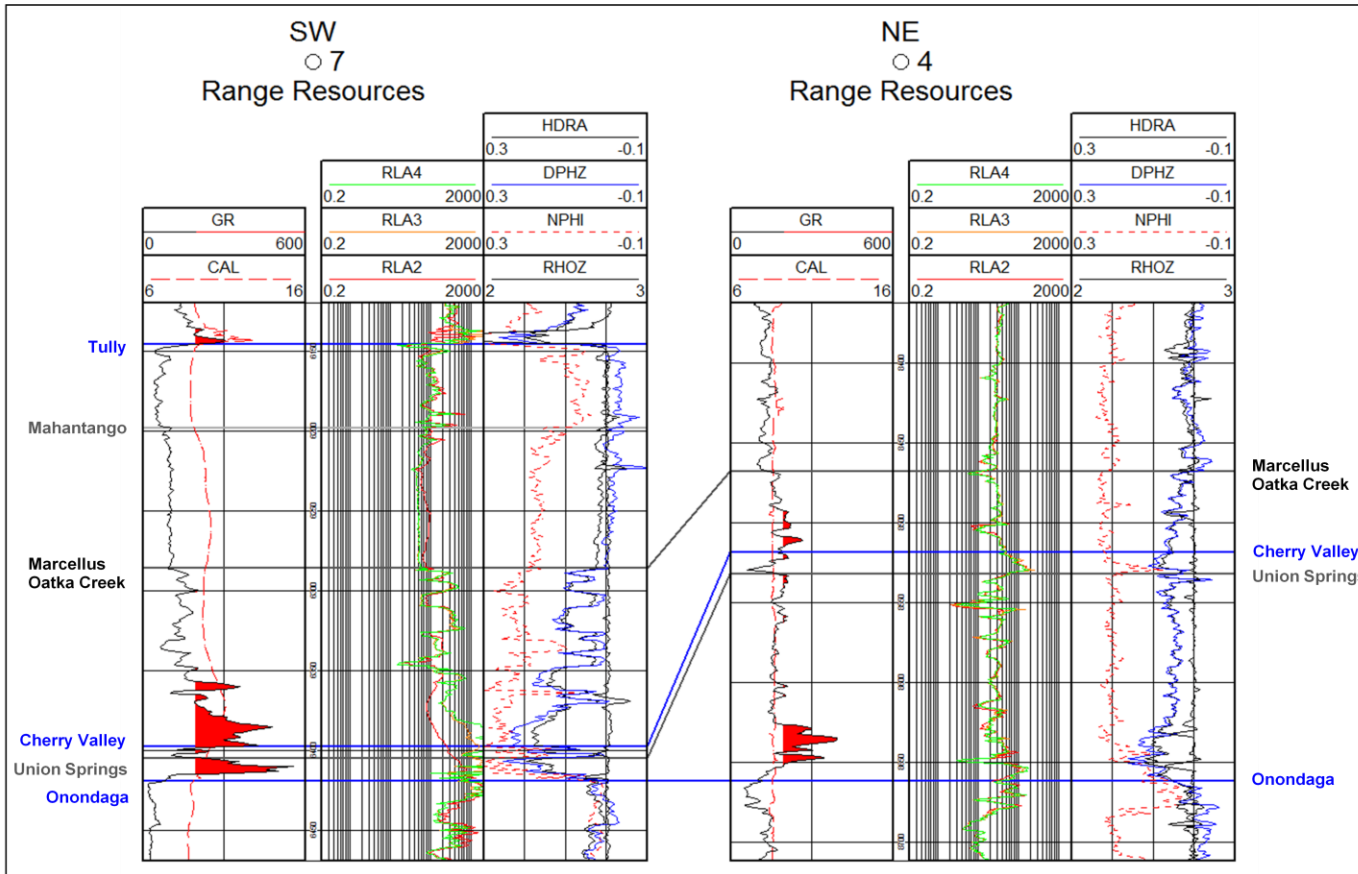


Figure 2-3 Type logs of Marcellus Formation from core production areas

Type logs from the Marcellus' two core production areas. The member names are shown at the top of the respective member. The Oatka Creek Member top is the same as the Marcellus top in the logs. The red gamma ray shading is to highlight GR API greater than 200 API and represents an Anoxic depositional setting.

The Union Springs and Oatka Creek members can both be described by a series of changes in depositional setting related to sea level change. These changes are a transgression systems tract (TST) and a high stand systems tract (HST), separated by a maximum flooding surface (MFS) (Lash and Engelder, 2009). The TST and MFS can be observed in Figure 2-3 on the gamma ray log as an increase in GR API moving up section with maximum API occurring at the MFS. During this event, the water column near the sediment was anoxic and a high concentration of organic deposition and preservation occurred (Wendt et al., 2015). It is in these zones of local higher GR API in Wendt et al's (2015) and my data set, that TOC vol% is higher compared to lower GR API zones. Anoxic conditions are represented on the type logs by a GR API shading in red of greater than 200 API. HST is a period of time when sea level likely remained constant, but periods of dysoxia occurred in the water column due to higher sediment influx resulting in lower concentrations of organic deposition and preservation (Wendt et al., 2015). GR API values for this depositional setting are lower than 200 API on the type logs.

Data in this study will be presented and compared in a variety of ways. Data presented concerning thermal maturity values will be divided and averaged by formation member. Thermal maturities may vary between the Union Springs and the Oatka Creek because the Union Springs was deposited below the Oatka Creek, being potentially subjected to greater thermal alteration. Visual comparisons within many of the graphs will be color coded by depositional setting. During anoxic deposition, the largest amounts of TOC were deposited. Since TOC is most likely the greatest control on the rock's ability to adsorb methane, this zone will be highlighted and compared against a dysoxic zone with lower TOC vol%.

Chapter 3

Previous Studies

There have been many studies involving adsorption of gas in shales due to its importance in evaluating reservoir gas-in-place. Results of these studies have yielded many shared observations of adsorptive storage capacity of methane in organic rich shales. All reviewed studies show a positive correlation between adsorptive storage capacity and TOC content (Chareonsuppanimit et al., 2012; Gasparik et al., 2014; Guo, 2013; Heller & Zoback, 2014; Lu et al., 1995; Ross & Bustin, 2009; Schettler et al., 1991; Zhang et al., 2012). Another variable controlling adsorptive storage capacity is thermal maturity. Gasparik et al. (2014), Heller & Zoback (2014), Ross & Bustin (2009), and Zhang et al. (2012) all observed that adsorptive storage capacity increased with maturity from immature to gas prone samples. However, Gasparik et al. (2014) and Zhang et al. (2012) both observed that adsorptive storage capacity decreased in samples considered to be over mature, above 2% V_{ROE} .

Heller & Zoback (2014), Ross & Bustin (2009), and Zhang et al. (2012) also found that pore composition and structure affects adsorptive storage capacity. Samples with many small pores have a large surface area which results in a large micropore volume of adsorbed gas. Higher quantities of gas can be adsorbed in under those conditions as opposed to large pores with less surface area. In addition to TOC content as the major controlling factor of adsorption, Lu et al. (1995), Ross & Bustin (2009), and Schettler et al. (1991) attribute a portion of total adsorption to other mineral constituents. Their findings all agreed that illite, the most common clay in their shales, is capable of adsorbing methane. Out of these eight studies, only two have data from the Marcellus shale. Heller & Zoback (2014) and Lu et al. (1995) both included Marcellus data in their papers, both samples contained very low TOC wt%, 1.2% and 1% respectively.

Chapter 4

Data Set

The data set for this study comes from a proprietary industry consortium. With permission from each well's operator and the proprietor of the consortium, data has been made available for this study on the condition that the identity of the operators and wells is kept anonymous. Well data includes wireline logs, methane adsorption isotherms, vitrinite reflectance estimations, TOC/Rock Eval Pyrolysis, and XRD. Figure 4-1 is a map of Pennsylvania with the general locations of the wells. Tables 4-1 through 4-5 contain the entire data set for reference. A dash in the table (–) means there was no sampled data for that depth point.

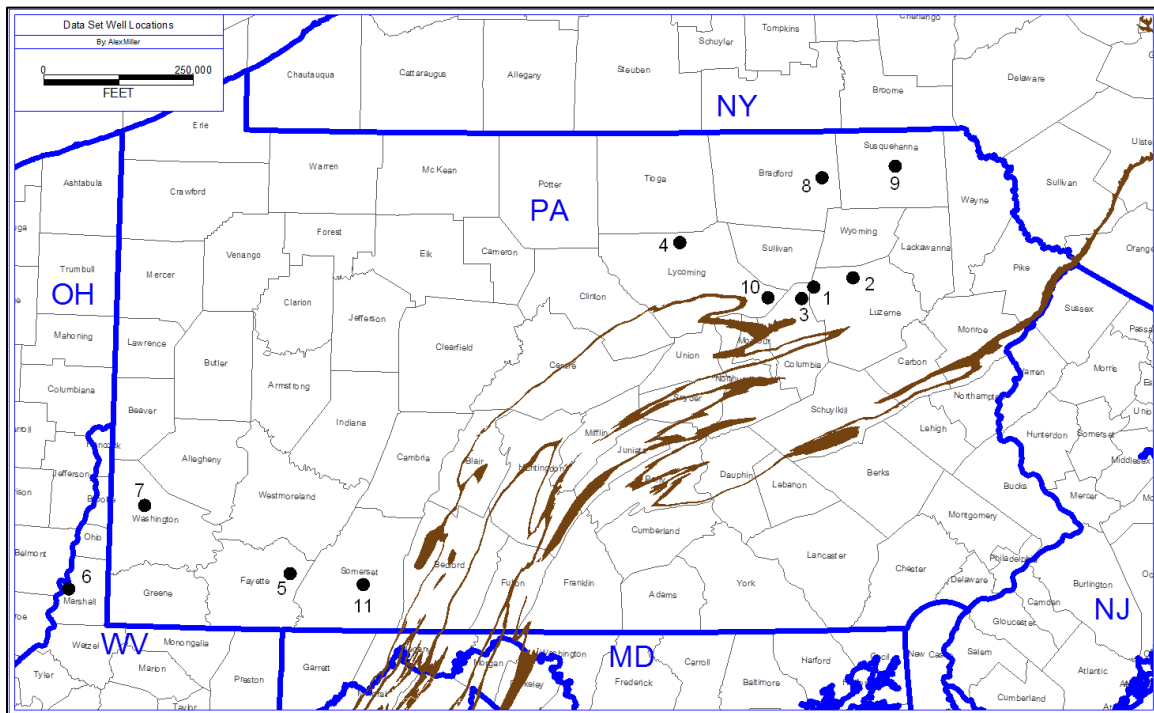


Figure 4-1 Map of study area with numbered data points

Black dots are wells where data points were collected. Data points are numbered by well code for data table. Blue outlines are states, black outlines are counties. Brown polygons are where the Marcellus Formation outcrops.

Table 4-1 Sample Number, Region, Well Code, Elevation, Sample Depth,
Subsea Depth, Formation Member, Depositional Setting, Isotherm Temperature,
G_S In-Situ Storage Capacity, P Reservoir Pressure, G_{SL} Langmuir Storage Capacity,
P_L Langmuir Pressure

Sample Number	Region	Well Code	Elev (KB or GL)	Sample Depth	Subsea Depth	Fm. Member	Depositional Setting	Isotherm Temperature Deg F	G _S In-Situ Storage Capacity scf/ton	P Reservoir Pressure psia	G _{SL} Langmuir Storage Capacity scf/ton	P _L Langmuir Pressure psia
1	NE	1	1263	7727.45	-6464.45	Oatka Creek	Dysoxic	178	39.73	3864	48.74	876.06
2	NE	1	1263	7865.05	-6602.05	Union Springs	Dysoxic	178	43.66	3933	51.00	660.92
3	NE	1	1263	7924.05	-6661.05	A	Anoxic	178	91.32	3962	102.14	469.22
4	NE	1	1263	7935.05	-6672.05	A	Anoxic	178	119.25	3968	135.73	548.33
5	NE	2	1384	7112.23	-5728.23	Oatka Creek	Dysoxic	168	49.53	3556	61.91	889.04
6	NE	2	1384	7180.6	-5796.6	Oatka Creek	Dysoxic	168	44.65	3590	58.21	1089.75
7	NE	3	906	5911	-5005	Oatka Creek	Dysoxic	120	55.42	3610	63.96	556.09
8	NE	3	906	5947.5	-5041.5	Union Springs	Dysoxic	120	56.09	3610	66.85	692.23
9	NE	3	906	6093	-5187	A	Anoxic	120	91.44	3610	100.97	376.32
10	NE	4	2287	8481.5	-6194.5	Oatka Creek	Dysoxic	133	54.98	5889	64.14	981.12
11	NE	4	2287	8539	-6252	Union Springs	Dysoxic	133	82.09	5889	90.18	580.88
12	NE	4	2287	8650.5	-6363.5	A	Anoxic	133	140.15	5889	149.73	402.54
13	SW	5	1432	7694	-6262	Oatka Creek	Dysoxic	154	72.28	4177	92.22	1152.12
14	SW	5	1432	7745.5	-6313.5	Union Springs	Dysoxic	154	109.91	4177	131.64	825.85
15	SW	5	1432	7772.5	-6340.5	A	Anoxic	154	185.66	4177	203.27	396.15
16	SW	6	1254	6349	-5095	Oatka Creek	Dysoxic	129	44.35	4060	60.84	1510.40
17	SW	6	1254	6360	-5106	Oatka Creek	Anoxic	129	103.30	4060	133.43	1184.33
18	SW	6	1254	6370.5	-5116.5	Oatka Creek	Anoxic	129	148.00	4060	188.85	1120.48
19	SW	7	1230	6341.9	-5111.9	Oatka Creek	Dysoxic	140	20.40	2760	60.10	5358.10
20	SW	7	1230	6365.8	-5135.8	Oatka Creek	Anoxic	140	87.20	2770	170.30	2639.60
21	SW	7	1230	6421.8	-5191.8	A	Anoxic	141	177.90	2795	297.00	1870.40
22	NE	8	1316	6369	-5053	Oatka Creek	Dysoxic	112	24.98	2882	36.78	1362.74
23	NE	8	1316	6420	-5104	Union Springs	Dysoxic	112	88.69	2882	126.65	1233.48
24	NE	8	1316	6480	-5164	A	Anoxic	112	151.41	2882	205.63	1032.25
25	NE	9	1540	6349.5	-4809.5	Oatka Creek	Dysoxic	109	58.11	2010	75.43	599.28
26	NE	9	1540	6589	-5049	Union Springs	Dysoxic	109	108.82	2010	134.90	481.77
27	NE	9	1540	6670	-5130	A	Anoxic	109	184.68	2010	236.74	566.57
28	NE	10	1126	6518	-5392	Union Springs	Dysoxic	110	77.70	3277	97.62	839.94
29	NE	10	1126	6558	-5432	Union Springs	Dysoxic	110	84.89	3277	105.55	797.61
30	NE	10	1126	6590	-5464	A	Anoxic	110	114.62	3277	131.41	480.07
31	SW	11	2370	8775.5	-6405.5	Oatka Creek	Dysoxic	166	54.32	3955	66.66	898.62
32	SW	11	2370	8800.5	-6430.5	Oatka Creek	Dysoxic	166	40.26	3975	57.83	1734.50
33	SW	11	2370	8850.5	-6480.5	Union Springs	Dysoxic	166	103.20	3997	136.84	1302.99
34	SW	11	2370	8880.5	-6510.5	A	Anoxic	166	190.99	4011	243.55	1103.80

Table 4-2 Normalized adsorption capacities (in-situ and Langmuir) by vol% and wt%

TOC, TOC vol%, TOC wt%, G_{SLM}, TOC_M, G_{SLM} with TOC_M

Sample Number	Region	Well Code	Normalized G _S /TOC Storage Capacity scf/(ton*toC vol)	Normalized G _{SL} /TOC Storage Capacity scf/(ton*toC vol)	TOC Vol%	G _{SLM} , Modeled Langmuir Storage Capacity scf/ton	TOC _M , Modeled TOC from U and Bulk Density	G _{SLM} , Modeled Langmuir Storage Capacity w/ TOC _M scf/ton	Normalized G _S /TOC Storage Capacity scf/(ton*toC wt)	Normalized G _{SL} /TOC Storage Capacity scf/(ton*toC wt)	TOC Wt%
1	NE	1	9.93	12.19	4.00	44.79	4.94	61.69	17.66	21.66	2.25
2	NE	1	6.93	8.10	6.30	67.25	6.51	75.31	12.55	14.66	3.48
3	NE	1	6.62	7.40	13.80	143.55	10.95	113.27	10.55	11.79	8.66
4	NE	1	8.52	9.70	14.00	146.12	9.12	97.17	12.70	14.45	9.39
5	NE	2	7.28	9.10	6.80	68.72	-	-	13.14	16.42	3.77
6	NE	2	7.83	10.21	5.70	56.82	-	-	13.95	18.19	3.20
7	NE	3	6.60	7.61	8.40	97.85	5.44	66.90	13.20	15.23	4.20
8	NE	3	8.13	9.69	6.90	77.19	7.08	80.88	14.68	17.50	3.82
9	NE	3	8.24	9.10	11.10	120.00	11.82	122.32	14.18	15.65	6.45
10	NE	4	12.79	14.92	4.30	67.33	5.26	69.45	23.70	27.65	2.32
11	NE	4	11.56	12.70	7.10	91.06	7.79	90.43	20.57	22.60	3.99
12	NE	4	12.19	13.02	11.50	133.50	14.25	145.79	17.63	18.83	7.95
13	SW	5	13.64	17.40	5.30	69.46	6.75	81.32	25.63	32.70	2.82
14	SW	5	12.35	14.79	8.90	108.21	8.90	101.59	21.26	25.46	5.17
15	SW	5	10.86	11.89	17.10	193.91	22.35	222.18	17.35	19.00	10.70
16	SW	6	6.08	8.33	7.30	117.44	9.10	110.55	9.77	13.40	4.54
17	SW	6	7.65	9.88	13.50	188.21	13.93	181.00	10.58	13.67	9.76
18	SW	6	7.51	9.59	19.70	253.47	13.93	180.98	10.28	13.11	14.40
19	SW	7	4.64	13.66	4.40	86.96	8.18	102.74	8.16	24.04	2.50
20	SW	7	8.99	17.56	9.70	143.18	9.41	129.07	14.25	27.83	6.12
21	SW	7	9.31	15.55	19.10	283.54	13.57	299.64	13.42	22.40	13.26
22	NE	8	10.86	15.99	2.30	54.06	-	-	19.83	29.19	1.26
23	NE	8	12.67	18.09	7.00	98.37	-	-	21.47	30.67	4.13
24	NE	8	11.74	15.94	12.90	158.78	-	-	17.79	24.16	8.51
25	NE	9	13.51	17.54	4.30	73.19	-	-	24.52	31.83	2.37
26	NE	9	12.65	15.69	8.60	115.49	-	-	22.03	27.31	4.94
27	NE	9	14.32	18.35	12.90	164.02	-	-	21.33	27.34	8.66
28	NE	10	12.14	15.25	6.40	85.06	-	-	21.17	26.60	3.67
29	NE	10	9.65	11.99	8.80	110.30	-	-	16.39	20.38	5.18
30	NE	10	9.63	11.04	11.90	141.19	-	-	15.74	18.05	7.28
31	SW	11	13.25	16.26	4.10	79.41	5.92	79.59	24.47	30.03	2.22
32	SW	11	14.38	20.65	2.80	68.05	3.63	63.76	27.58	39.61	1.46
33	SW	11	13.23	17.54	7.80	116.78	6.97	91.60	23.72	31.46	4.35
34	SW	11	14.36	18.31	13.30	175.72	13.00	151.23	23.99	30.60	7.96

Table 4-3 Pyrolysis results, Thermal maturity (V_{ROE}) whole well & by formation member, Deep resistivity (ohm*m), Uranium (ppm), Gamma Ray (API)

Sample Number	Region	Well Code	S1 mg HC/g	S2 mg HC/g	S3 mg CO2/g	Tmax deg c	HI S2x100/TOC	OI S3x100/TOC	PI S1/(S1+S2)	Average V_{ROE} Whole Well	Average V_{ROE} Fm Member	Deep Resistivity ohmm	Uranium ppm	Gamma Ray API
1	NE	1	0.65	0.62	0.13	320	27.56	5.78	0.51	3.71	3.65	0.44	6.51	117.72
2	NE	1	0.51	0.59	0.11	308	16.95	3.16	0.46	3.71	3.79	0.12	11.58	162.90
3	NE	1	0.18	0.62	0.54	362	7.16	6.24	0.23	3.71	3.79	0.12	26.57	255.88
4	NE	1	0.33	0.98	0.47	343	10.44	5.01	0.25	3.71	3.79	0.07	20.55	220.19
5	NE	2	0.03	0.07	0.07	382	1.86	1.86	0.30	3.98	3.98	0.28	-	169.41
6	NE	2	0.22	0.51	0.25	400	15.94	7.81	0.30	3.98	3.98	0.21	-	134.11
7	NE	3	0.10	0.11	0.46	-	3.00	11.00	0.48	3.36	3.10	0.64	8.49	139.46
8	NE	3	0.10	0.07	0.47	-	1.00	10.00	0.59	3.36	3.49	0.88	13.61	180.37
9	NE	3	0.15	0.12	0.71	-	1.00	5.00	0.56	3.36	3.49	0.33	29.34	251.89
10	NE	4	0.09	0.12	0.03	-	6.00	1.00	0.43	2.58	2.40	27.50	7.60	161.61
11	NE	4	0.12	0.11	0.13	-	2.00	3.00	0.52	2.58	2.76	17.68	15.90	212.67
12	NE	4	0.22	0.32	0.13	-	4.00	2.00	0.41	2.58	2.76	11.49	37.62	332.46
13	SW	5	0.07	0.09	0.16	-	3.00	5.00	0.44	2.93	2.95	39.85	12.47	164.43
14	SW	5	0.11	0.17	0.32	-	3.00	5.00	0.39	2.93	2.90	78.25	19.56	233.83
15	SW	5	0.15	0.35	0.52	-	3.00	5.00	0.30	2.93	2.90	117.75	63.66	658.67
16	SW	6	2.55	2.52	0.29	461	72.00	8.00	0.50	1.00	1.00	160.00	20.92	273.38
17	SW	6	-	-	-	-	-	-	-	1.00	1.00	1050.00	37.40	361.47
18	SW	6	9.53	15.78	0.40	457	101.00	3.00	0.38	1.00	1.00	1060.00	37.50	378.70
19	SW	7	-	-	-	-	-	-	-	1.31	1.31	122.02	17.00	80.60
20	SW	7	3.22	3.21	0.24	466	52.00	4.00	0.50	1.31	1.31	672.24	22.00	161.49
21	SW	7	-	-	-	-	-	-	-	1.31	1.32	4717.23	36.00	331.52
22	NE	8	-	-	-	-	-	-	-	2.06	2.02	244.41	-	105.82
23	NE	8	0.11	0.12	0.34	-	3.00	8.00	0.48	2.06	2.08	58.91	-	261.54
24	NE	8	-	-	-	-	-	-	-	2.06	2.08	140.51	-	575.89
25	NE	9	0.04	0.05	0.11	-	2.00	5.00	0.44	2.11	2.09	109.28	-	170.31
26	NE	9	0.04	0.11	0.31	-	3.00	7.00	0.27	2.11	2.18	154.61	-	341.20
27	NE	9	0.07	0.17	0.16	-	2.00	2.00	0.29	2.11	2.18	278.32	-	152.61
28	NE	10	0.13	0.00	0.14	-	0.00	4.00	1.00	2.66	2.66	5.57	-	201.49
29	NE	10	0.10	0.00	0.03	-	0.00	1.00	1.00	2.66	2.66	4.07	-	246.47
30	NE	10	0.10	0.00	0.33	-	0.00	4.00	1.00	2.66	2.66	1.98	-	293.27
31	SW	11	-	-	-	-	-	-	-	1.59	1.48	65.16	9.85	225.98
32	SW	11	-	-	-	-	-	-	-	1.59	1.48	188.89	2.19	106.79
33	SW	11	-	-	-	-	-	-	-	1.59	1.66	167.75	13.28	228.48
34	SW	11	-	-	-	-	-	-	-	1.59	1.66	362.57	33.19	361.45

Table 4-4 Mineralogies from XRD in wt%

Sample Number	Region	Well Code	Quartz Wt%	K Feldspar Wt%	Plagioclase Wt%	Calcite Wt%	Dolomite Wt%	Pyrite Wt%	Illite & Mica Wt%	Chlorite Wt%	Total Clay Wt%
1	NE	1	30.80	1.90	10.10	6.70	0.00	3.40	31.87	15.13	47.00
2	NE	1	33.00	1.90	10.30	2.00	0.00	7.10	38.85	6.86	45.70
3	NE	1	34.70	1.90	11.10	15.60	0.00	9.90	24.52	2.28	26.80
4	NE	1	43.70	0.60	7.20	25.90	0.00	4.60	15.07	2.93	18.00
5	NE	2	29.00	0.90	11.90	1.10	0.00	6.00	35.14	15.86	51.00
6	NE	2	26.60	1.80	9.50	19.90	0.00	2.50	26.49	13.11	39.60
7	NE	3	25.00	0.60	8.90	3.70	0.00	31.10	20.63	8.88	30.30
8	NE	3	30.20	0.40	9.30	11.60	0.00	7.70	27.36	12.24	39.60
9	NE	3	40.10	0.30	7.60	26.40	0.00	7.80	13.32	4.28	17.60
10	NE	4	40.80	0.00	5.50	0.40	0.00	8.50	30.69	14.11	44.80
11	NE	4	39.10	0.00	6.70	3.80	2.00	12.30	31.62	4.48	36.10
12	NE	4	70.90	0.00	3.20	1.20	4.10	6.60	14.00	0.00	14.00
13	SW	5	38.20	0.60	5.10	0.00	0.50	9.50	36.35	9.55	45.90
14	SW	5	46.40	0.50	4.20	10.30	0.90	9.40	26.61	1.79	28.40
15	SW	5	32.80	0.00	2.90	18.50	3.00	24.70	18.10	0.00	18.10
16	SW	6	31.20	0.00	5.20	0.70	1.10	6.30	50.45	5.05	55.50
17	SW	6	34.00	0.39	4.30	0.00	1.97	8.11	42.42	8.81	51.23
18	SW	6	34.20	1.30	4.90	5.00	4.30	17.00	33.30	0.00	33.30
19	SW	7	28.40	1.50	3.20	24.50	2.40	5.10	27.90	7.00	34.90
20	SW	7	51.70	0.00	2.30	4.20	1.90	15.00	20.29	4.61	24.90
21	SW	7	42.20	1.30	3.90	15.80	6.80	8.70	20.60	0.70	21.30
22	NE	8	30.60	0.00	4.20	38.70	4.40	3.50	17.40	1.20	18.60
23	NE	8	37.10	0.00	7.40	4.60	4.70	7.90	33.48	4.82	38.30
24	NE	8	52.00	0.00	5.50	13.00	1.30	10.00	18.20	0.00	18.20
25	NE	9	37.20	0.60	7.40	0.00	7.70	4.90	29.92	12.28	42.20
26	NE	9	40.60	0.00	10.10	2.10	1.60	14.40	31.10	0.00	31.10
27	NE	9	51.60	0.00	5.20	33.30	2.10	3.00	4.90	0.00	4.90
28	NE	10	40.80	0.00	10.00	5.30	0.00	5.30	26.02	12.58	38.60
29	NE	10	41.30	0.50	9.90	1.50	0.00	6.50	29.10	11.10	40.20
30	NE	10	42.40	0.00	8.00	12.70	0.70	8.90	24.40	2.80	27.20
31	SW	11	37.40	0.00	3.90	0.00	0.80	9.90	35.51	12.49	48.00
32	SW	11	36.10	0.00	6.60	7.20	1.70	10.90	32.42	5.08	37.50
33	SW	11	38.50	0.00	4.90	8.50	1.40	8.40	31.98	6.32	38.30
34	SW	11	35.90	0.00	3.40	17.00	2.80	7.80	28.05	5.05	33.10

Table 4-5 Mineralogies from XRD in vol%, Porosity %, Bulk Density (g/cc)

Sample Number	Region	Well Code	Quartz Vol%	K Feldspar Vol%	Plagioclase Vol%	Calcite Vol%	Dolomite Vol%	Pyrite Vol%	Illite & Mica Vol%	Chlorite Vol%	TOC Vol%	Clay Vol%	Porosity %	Bulk Density g/cm ³
1	NE	1	29.30	1.90	9.40	6.20	0.00	1.70	28.10	13.80	4.00	41.90	5.60	2.67
2	NE	1	31.60	1.90	9.70	1.90	0.00	3.60	34.50	6.30	6.30	40.80	4.30	2.68
3	NE	1	29.30	1.70	9.20	12.80	0.00	4.40	19.20	1.80	13.80	21.00	7.70	2.53
4	NE	1	34.50	0.50	5.60	19.90	0.00	1.90	11.10	2.20	14.00	13.30	10.30	2.55
5	NE	2	27.80	0.90	11.20	1.00	0.00	3.00	31.20	14.60	6.80	45.80	3.40	2.64
6	NE	2	25.20	1.80	8.80	18.30	0.00	1.20	23.20	11.90	5.70	35.10	3.90	2.63
7	NE	3	26.50	0.70	9.30	3.80	0.00	17.40	20.20	9.00	8.40	29.20	4.70	2.57
8	NE	3	29.00	0.40	8.80	10.80	0.00	3.90	24.30	11.20	6.90	35.50	4.70	2.63
9	NE	3	36.50	0.30	6.80	23.30	0.00	3.70	11.20	3.70	11.10	14.90	3.40	2.55
10	NE	4	40.30	0.00	5.30	0.40	0.00	4.40	28.10	13.30	4.30	41.40	3.90	2.65
11	NE	4	37.10	0.00	6.20	3.50	1.80	6.10	27.80	4.10	7.10	31.90	6.30	2.64
12	NE	4	54.40	0.00	2.40	0.90	2.90	2.70	9.90	0.00	11.50	9.90	15.30	2.45
13	SW	5	37.80	0.60	5.00	0.00	0.50	5.00	33.30	9.00	5.30	42.30	3.50	2.65
14	SW	5	42.30	0.50	3.80	9.20	0.80	4.50	22.50	1.50	8.90	24.00	6.00	2.62
15	SW	5	27.80	0.00	2.40	15.30	2.40	10.90	14.20	0.00	17.10	14.20	9.90	2.54
16	SW	6	26.70	0.00	4.40	0.60	0.90	2.80	40.00	4.10	7.30	44.10	13.20	2.43
17	SW	6	24.90	0.30	3.10	0.00	1.30	3.10	28.80	6.20	13.50	35.00	18.80	2.22
18	SW	6	24.80	1.00	3.50	3.50	2.90	6.50	22.40	0.00	19.70	22.40	15.70	2.19
19	SW	7	26.70	1.50	2.90	22.30	2.10	2.50	24.30	6.30	4.40	30.60	7.00	2.68
20	SW	7	43.50	0.00	1.90	3.40	1.50	6.60	15.80	3.80	9.70	19.60	13.80	2.41
21	SW	7	32.40	1.00	2.90	11.80	4.80	3.60	14.60	0.50	19.10	15.10	9.30	2.28
22	NE	8	30.00	0.00	4.00	37.00	4.00	1.80	15.80	1.20	2.30	17.00	3.90	2.64
23	NE	8	33.50	0.00	6.60	4.00	3.90	3.80	27.90	4.30	7.00	32.20	9.00	2.52
24	NE	8	41.90	0.00	4.30	10.20	1.00	4.20	13.70	0.00	12.90	13.70	11.80	2.38
25	NE	9	35.70	0.60	7.00	0.00	6.80	2.50	26.60	11.20	4.30	37.80	5.30	2.66
26	NE	9	37.40	0.00	9.20	1.90	1.40	7.00	26.60	0.00	8.60	26.60	7.90	2.55
27	NE	9	40.80	0.00	4.00	25.70	1.50	1.30	3.60	0.00	12.90	3.60	10.20	2.62
28	NE	10	37.90	0.00	9.10	4.80	0.00	2.60	22.40	11.20	6.40	33.60	5.60	2.64
29	NE	10	37.40	0.50	8.80	1.30	0.00	3.10	24.40	9.60	8.80	34.00	6.10	2.63
30	NE	10	36.90	0.00	6.80	10.80	0.60	4.10	19.60	2.30	11.90	21.90	7.00	2.54
31	SW	11	36.90	0.00	3.80	0.00	0.80	5.10	32.40	11.80	4.10	44.20	5.10	2.63
32	SW	11	36.50	0.00	6.50	7.10	1.60	5.80	30.40	4.90	2.80	35.30	4.40	2.68
33	SW	11	36.60	0.00	4.60	7.90	1.10	4.20	28.10	5.70	7.80	33.80	4.00	2.62
34	SW	11	31.90	0.00	3.00	14.70	2.20	3.70	23.10	4.30	13.30	27.40	3.80	2.55

Chapter 5

Methods

Methane Adsorption Isotherm

Adsorption is the process in which gas molecules condense and remain on a solid surface due to surface forces (Langmuir, 1918). Weak van der Waal's forces allow adsorption and desorption to occur readily on the sorbent. On the surface of the sorbent, receptor sites for the adsorbate (methane) can only accept one molecule. When pressure increases, more sites on the adsorbent become occupied until the sample is saturated. The layer of adsorbed molecules is only one molecule thick (Langmuir, 1918). Adsorption of methane by shales in unconventional reservoirs is one of two main gas storing mechanisms, the other being free gas in pore spaces (Ambrose et al., 2012). The Langmuir isotherm is used to measure adsorption on shales because of its simplicity and because the Langmuir model is a very good fit to the data (Heller and Zoback, 2014).

The Langmuir isotherm relationship is:

$$G_S = \frac{G_{SL} * P}{(P_L + P)} \dots \dots \dots (1a)$$

Or

$$G_S = \frac{G_{SL}}{\left(\frac{P_L}{P} + 1\right)} \dots \dots \dots (1b)$$

G_S – Gas Storage Capacity, *in-situ*, scf/ton

G_{SL} – Langmuir Storage Capacity, scf/ton

P_L – Langmuir Pressure, psia

P – Reservoir Pressure, psia (Ambrose et al, 2012)

Langmuir storage capacity (G_{SL}) is the maximum storage capacity, occurring at infinite pressure. The G_{SL} is the volume that is used in this paper for comparison purposes because it represents the volume at infinite pressures. This representation normalizes the samples because

the adsorption procedure is conducted at reservoir pressures, which can vary greatly from sample to sample. Langmuir Pressure (P_L) is the pressure at which storage capacity is half of the G_{SL} . G_{SL} and P_L are specific constants for each sample.

Equation 1b shows that as P gets larger, $G_S \rightarrow G_{SL}$. Also, when $P = 0$, $G_S = 0$.

The linear form of the Langmuir relationship is:

$$\frac{P}{G_S} = \frac{1}{G_{SL}} * P + \frac{P_L}{G_{SL}} \dots\dots\dots(2) \text{ (Hartman, 2012)}$$

Shown in Equation 3 is it's relation to the linear equation $y = mx + b$ where $y = P/G_S$;

$x = P$; $m = 1/G_{SL}$; and $b = P_L/G_{SL}$.

$$\frac{P}{G_S} = \frac{1}{G_{SL}} * P + \frac{P_L}{G_{SL}}$$

$$y = m * x + b \dots\dots\dots(3)$$

In the laboratory, G_S is measured from various values of P . The slope of a linear regression of P/G_S vs. P is $1/G_{SL}$. The intercept is P_L/G_{SL} , so both G_{SL} and P_L can be found for that particular sample.

The measurement process of methane adsorption is summarized as follows from Weatherford Laboratories (Hartman, 2012): all rock is prepared and tested, as received from core. A 100 gram sample is crushed down to a particle size of 60 mesh, or 250 μm . Figure 5-1 is a basic diagram of the isotherm testing setup. The crushed shale sample is then put into the sample container and weighed to the 1000th of a gram. After sealing the sample container, a dead space volume is measured using helium gas expansion, since helium is a non-adsorbing gas. Volumes are measured with a precision of .03cc. The entire system is then pressurized to reservoir pressure with helium to ensure no leaks. Once the system is determined to be leak free, helium is removed. To begin the isotherm test, with the valve between the reference and sample cells closed, the reference cell is pressurized with methane and the pressure is recorded. Next,

the valve between the reference and sample is opened, allowing the sample cell to increase in pressure while the reference cell decreases in pressure. The valve is shut as the pressures near each other, but with the sample cell's pressure slightly lower than the reference. Over a period of time, pressure in the reference cell remains constant, while pressure in the sample cell decreases then stabilizes. The pressure decrease in the sample chamber represents the conversion of free gas in the sample chamber to adsorbed gas on the shale sample. The stabilization of pressure means no more gas is adsorbing at that pressure. Using the real gas law, the volume of methane adsorbed can be calculated from the difference in void volume of the system before the pressure step, and after the pressure step. Gas storage capacity is initially calculated in cm^3/g , and can be converted to scf/ton by multiplying cm^3/g by 32.036929 (Hartman, 2012). This series of steps is repeated on average 6 more times, increasing the initial pressure of the reference cell each step until reservoir pressure is reached.

The main source of error in measuring the adsorption isotherm is maintaining a system temperature within 0.1°C of the required temperature. Changes in temperature will affect the volume of adsorbed methane (Guo, 2013). Maintaining the temperature in the room is as important as maintaining temperature in the oil bath in which the measurement is made. Other sources of error lie in the calibration of the electronic equipment. Sample weights are measured to 0.001 g, and the volume transducer must measure to .033cc. If these tools are not calibrated correctly, measurements will be unrepresentative of the true sample. Acknowledging these challenges in laboratory consistency, the laboratory claims a 95% confidence interval in all of their adsorption isotherm measurements.

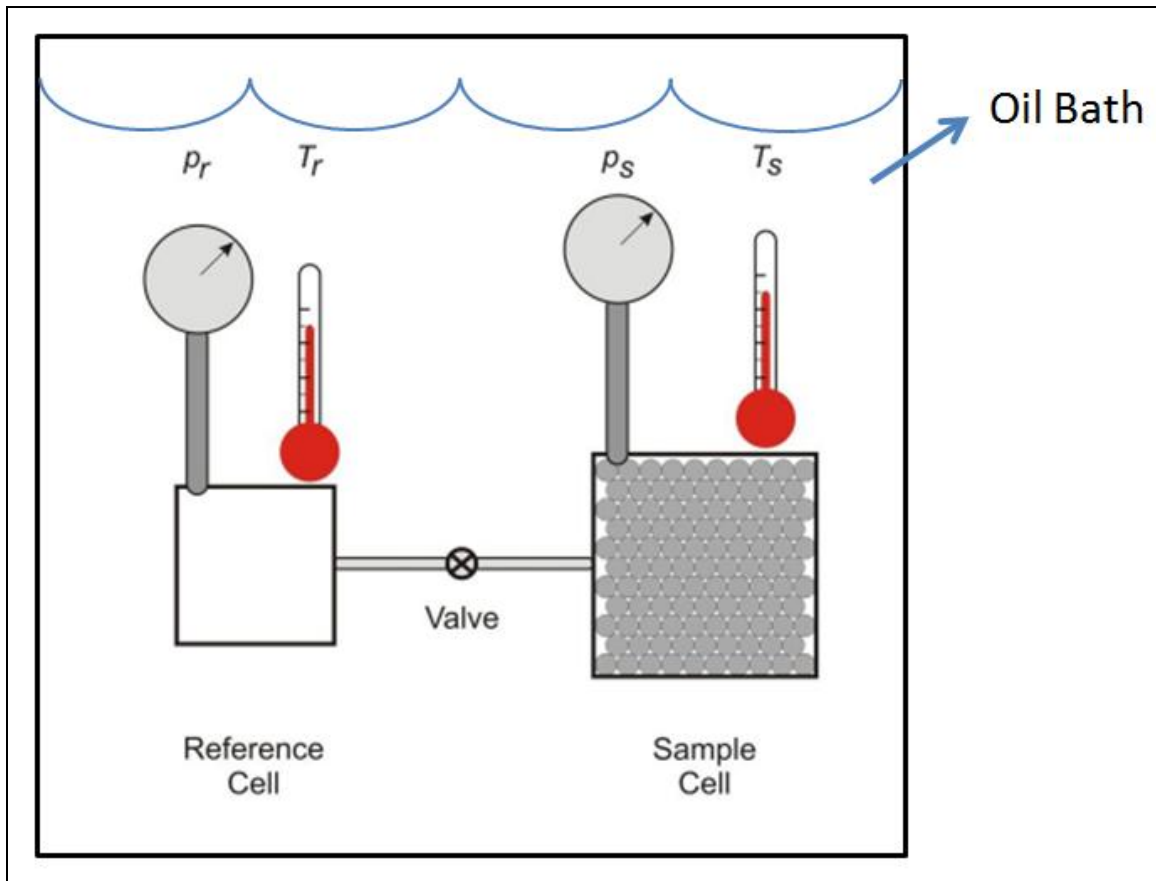


Figure 5-1 Generalized setup for adsorption isotherm testing

Modified from Hartman (2012) is a generalized setup for the adsorption isotherm test. Entire testing schematic is submerged in an oil bath to maintain constant temperature to simulate in-situ reservoir conditions.

Thermal Maturity

Thermal maturity of a source rock is used to estimate the volume of hydrocarbons that have been generated (Peters, 1986). Source rocks of low thermal maturity have generated minimal amounts of hydrocarbons and have potential to generate more if subjected to more heating. Source rocks of high thermal maturity have generated most or all of their hydrocarbons. Thermal maturity is most commonly evaluated by a combination of programmed pyrolysis and vitrinite reflectance. In this study, the Marcellus Formation is represented by two members, the Union Springs and the Oatka Creek. Thermal maturity values will be separated by formation member. Figure 5-2 shows the two members highlighted on the type logs.

Programmed Pyrolysis

The following description of programmed pyrolysis using Rock-Eval is summarized from Peters (1986) and Hart and Steen (2015): Rock-Eval pyrolysis evaluates thermal maturity of a source rock by heating crushed samples in an inert atmosphere. The sample is heated at 300°C for a set period of time until all of the insitu hydrocarbons are cooked off. The temperature is then increased at a rate of 25°C/min until temperature reaches 600°C. During this time, hydrocarbons are generated from the sample due to heating. Once the system reaches 600°C, temperature cools and a measurement of CO₂ produced is taken.

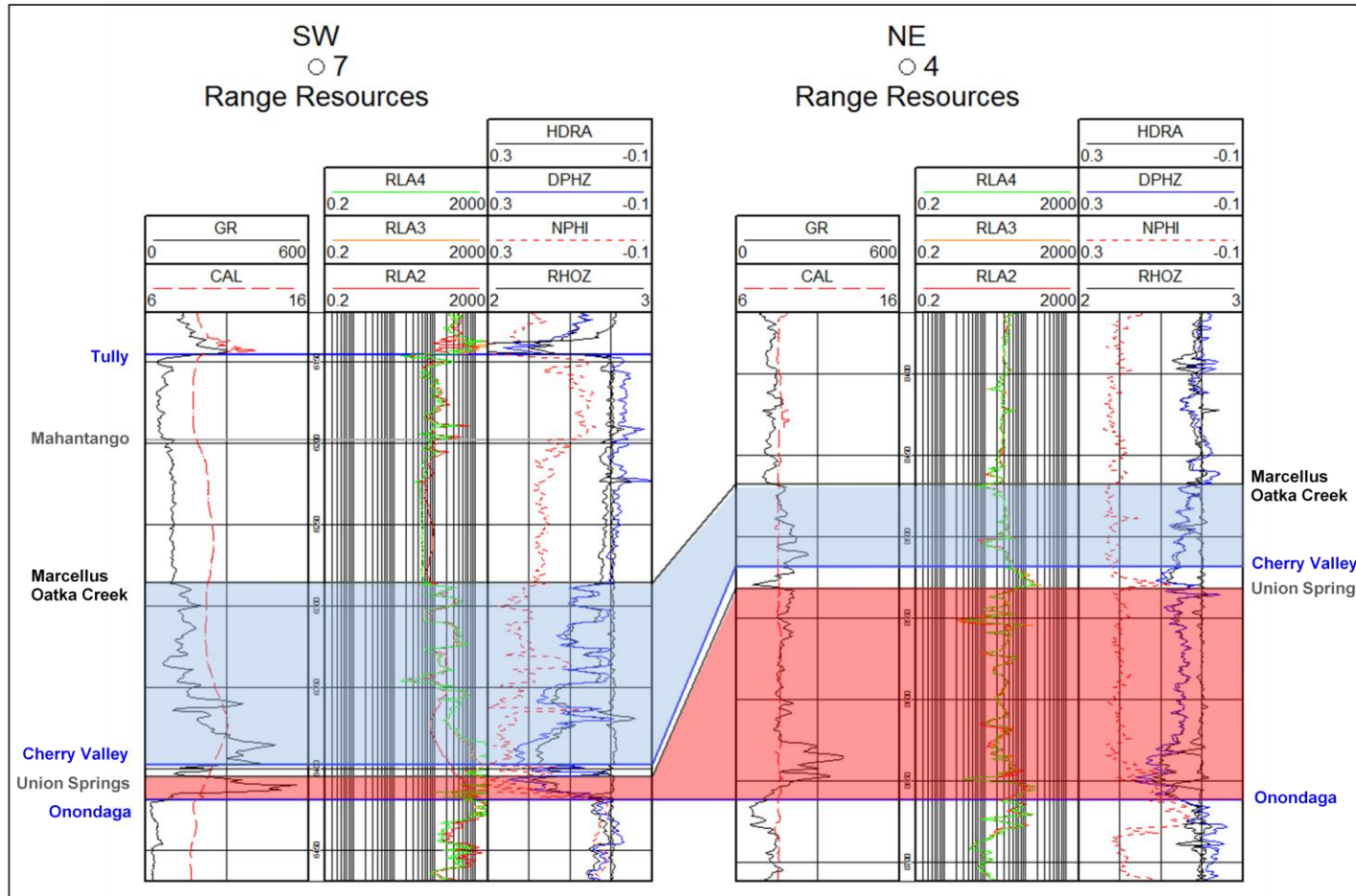


Figure 5-2 Type logs of Marcellus Formation from core production areas

Members of the Marcellus highlighted for maturity evaluation. The Oatka Creek member is highlighted in blue and the Union Springs member is highlighted in red.

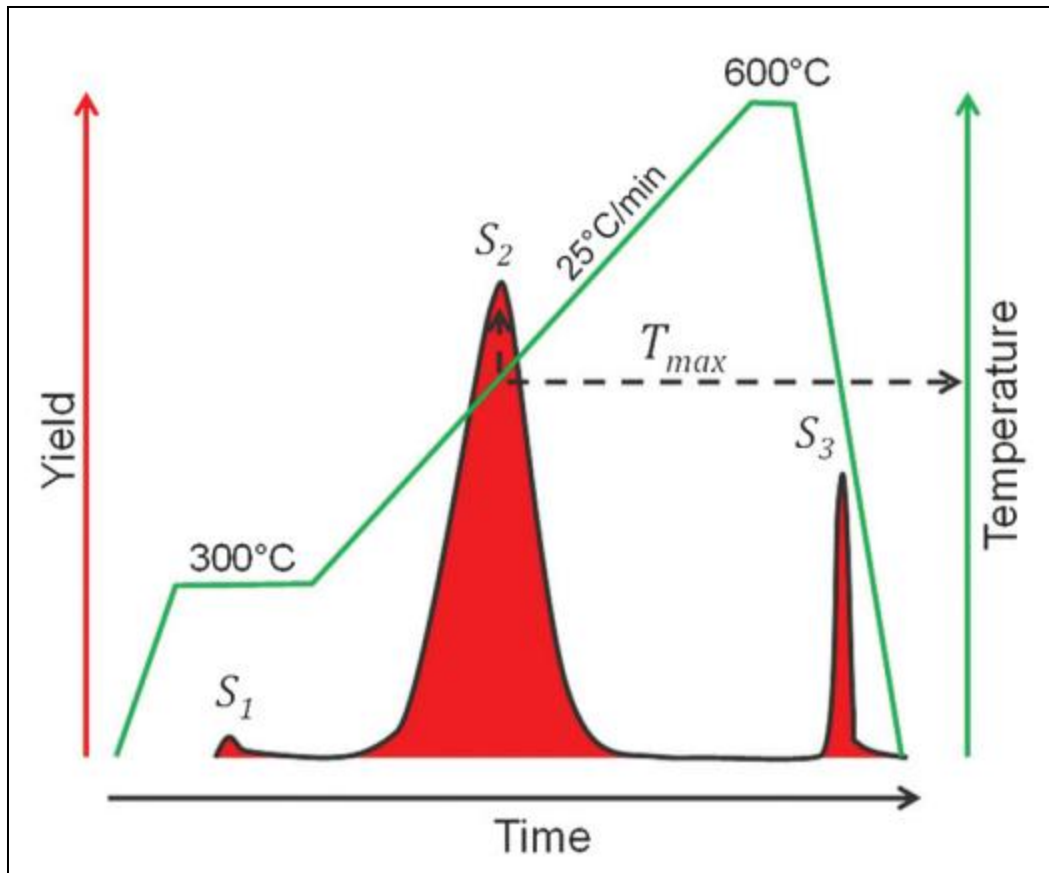


Figure 5-3 Programmed Pyrolysis responses

Diagram of typical programmed pyrolysis responses during heating of rock sample (Hart and Steen, 2015). The green curve is change in temperature with time. The S₁ peak measures hydrocarbons previously generated in the sample. The S₂ peak represents hydrocarbons generated during heating of the sample. The S₃ peak represents carbon dioxide from cracking of residual kerogen. T_{max} is the temperature at which the S₂ peak occurs.

Figure 5-3 is an image of a standard pyrogram from Hart and Steen (2005). Five measurements take place during the pyrolysis procedure. The first measurement is S₁ (mg HC/g rock), represents how many hydrocarbons are contained, already generated, in the rock. The second measurement, S₂ (mg HC/g rock), represents hydrocarbons generated from pyrolysis, or the generative potential if the source rock were to continue heating in-situ. The third

measurement, S3 (mg CO₂/g rock), represents CO₂ generated during pyrolysis as a result of thermal cracking of kerogen. The fourth measurement, T_{max}, is the temperature at which the maximum S₂ occurs (the peak). This value can be used to evaluate the thermal maturity of organic matter, but if a low S₂ peak occurs, T_{max} can be unrepresentative. In this study, due to low S₂ values, T_{max} is rendered un-useable as a maturity evaluator. The fifth measurement is S₄. Once pyrolysis is complete, the sample is oxidized, and the residual carbon of the sample is measured. This carbon is highly condensed and represents organics that may have once generated hydrocarbons. The addition of S₁ (mg HC/g rock), S₂ (mg HC/g rock), and the final residual carbon S₄ are summed to get a TOC weight percent (wt%) (Jarvie, 1991; Hart and Steen, 2015). For the purposes of this paper, TOC volume percent (vol%) will be used instead of a wt%. Because it has a low density, TOC volume is more representative of its contribution to the entire mineral assemblage of the rock. Volume is also used because it is compared to a volume of gas that is adsorbed on a volume of organics. Figure 5-4 is the comparison of TOC vol% vs. TOC wt%, showing vol% to be an average 1.55x wt%.

One method of evaluating thermal maturity using programmed pyrolysis data is plotting a Hydrogen Index vs. an Oxygen Index of multiple samples. A Pseudo Van Krevlin diagram is a plot of HI (S₂/TOC) x100 on the Y axis, and OI (S₃/TOC) x100 on the X axis (Figure 5-5, Hart and Steen, 2015). This type of graph is typically used to evaluate kerogen types, but can also evaluate maturity because samples will decrease in HI and OI with increasing maturity (Nordeng, 2012). Figure 5-6 is a pseudo Van Krevlin diagram of my data set. All but three of the points have an S₂ value lower than 1, resulting in very low HI values. When S₂ values are less than 2.5 the source rock has poor potential for generating additional hydrocarbons (Peters, 1986). It is clear that all but three of the samples are very mature, but are indistinguishable due to their small deviation in HI.

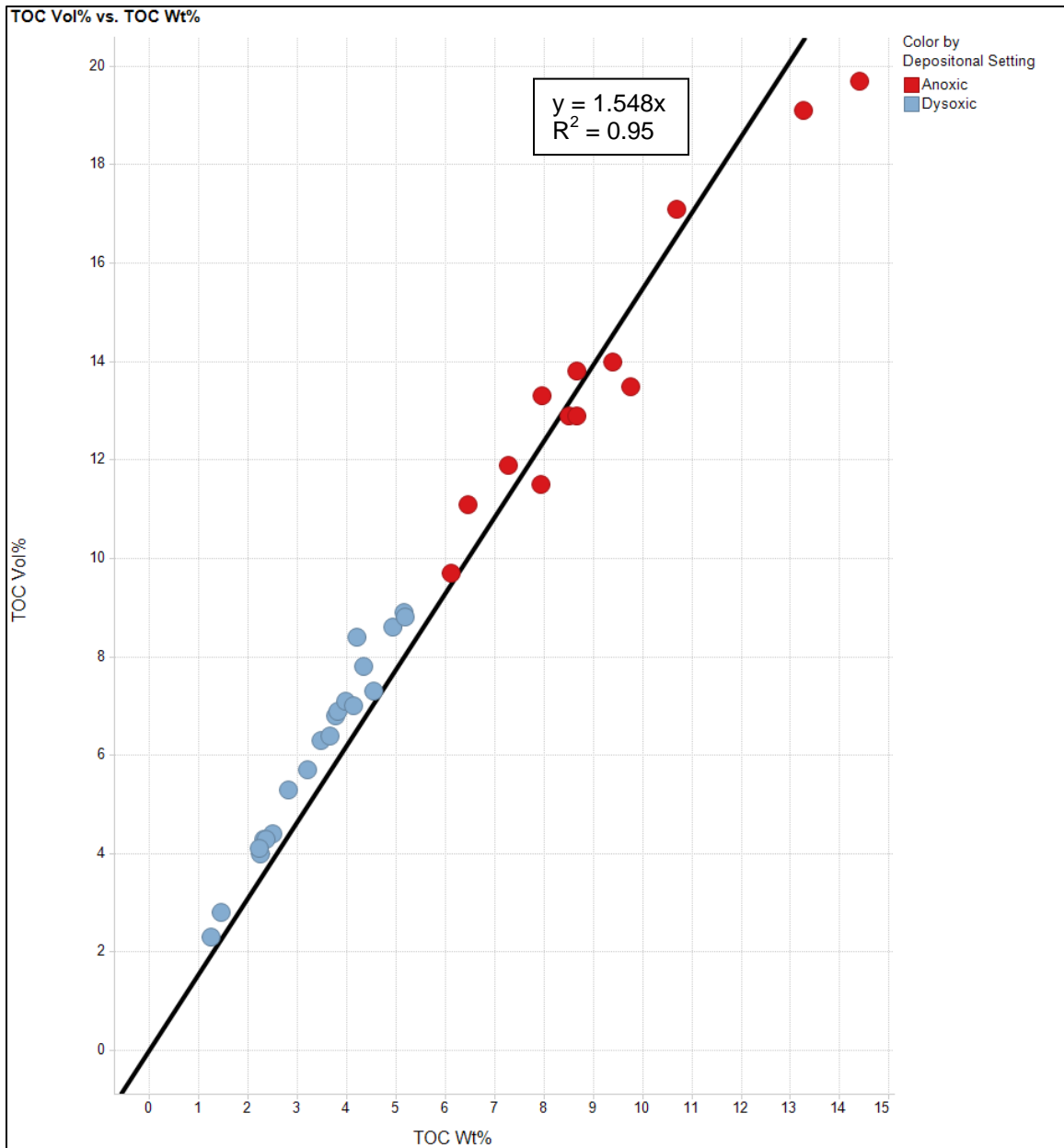


Figure 5-4 TOC vol% vs. TOC wt%

TOC vol% vs. TOC wt%. plotted from data in Table II. TOC vol% is shown to be greater than TOC wt% by an average factor of about 1.55x TOC wt%. Color coding is by depositional setting: anoxic is red and dysoxic is blue.

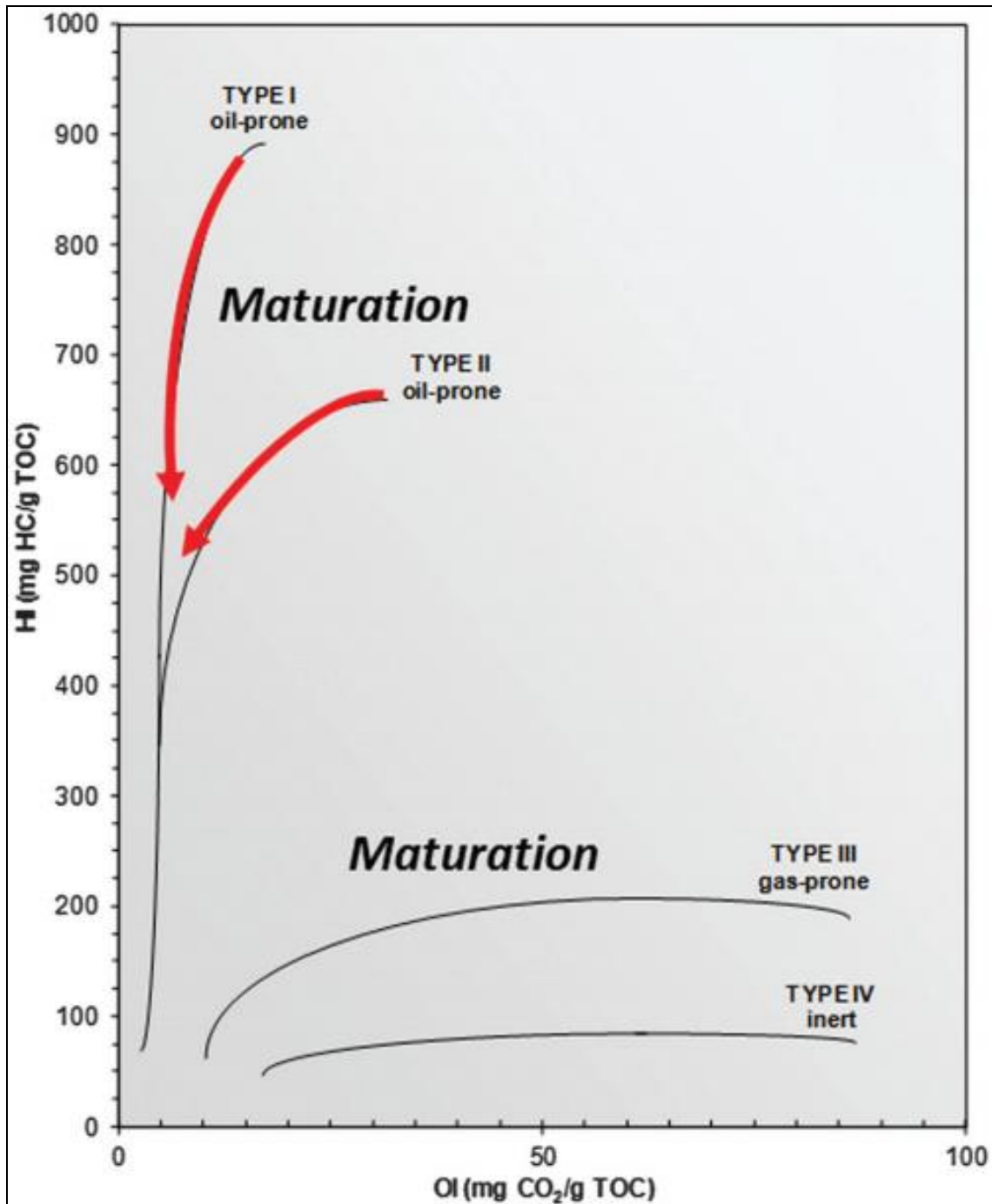


Figure 5-5 Pseudo Van Krevlin diagram highlighting maturity trends

Pseudo Van Krevlin diagram from Hart and Steen (2015). Figure plots HI vs. OI and evaluates maturity by decreases in HI and OI.

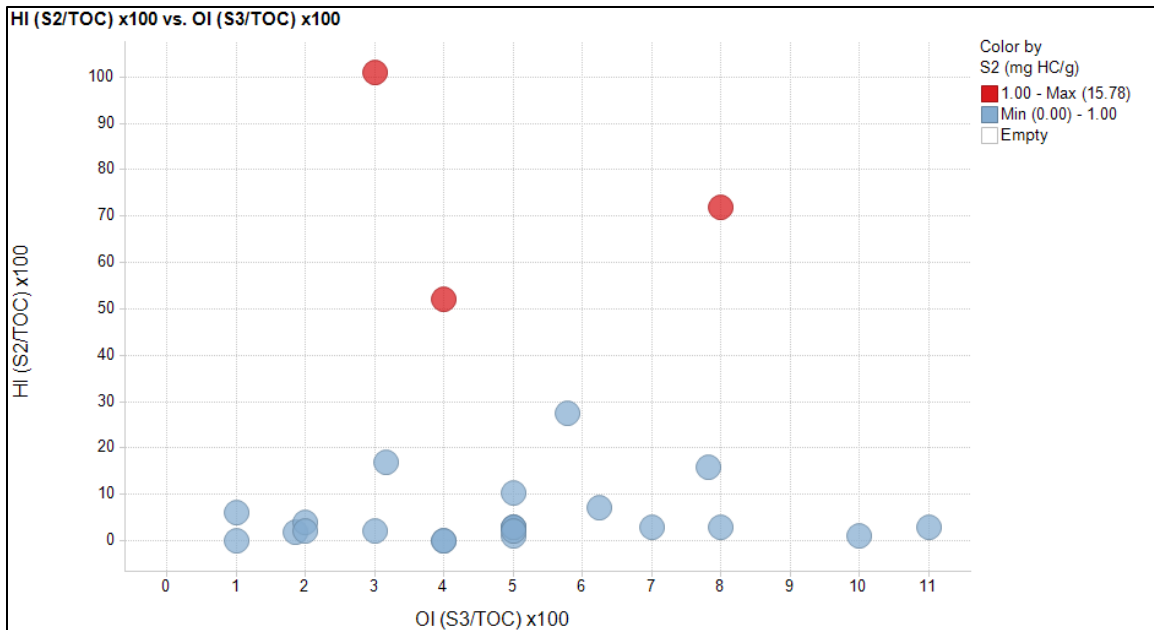


Figure 5-6 Pseudo Van Krevlin diagram for data set

Pseudo Van Krevlin diagram from data set. This is a poor method of maturity evaluation for this data set due to the low S2 numbers and the majority of the data set indistinguishable due to low HI values.

Vitrinite Reflectance

The second common evaluator of thermal maturity is vitrinite reflectance (V_{RO}). An organic petrographer evaluates the maturity of a source rock by measuring the reflectance of vitrinite particles. Vitrinite is the plant derived kerogen of a source rock. The Marcellus Shale however, contains mainly algal organic macerals instead of vitrinite. Reflectance relationship methods, such as used by Petersen et al. (2013) and Repetski et al. (2002), measure reflectance of other organic matter and relate it to a corresponding vitrinite reflectance. Vitrinite reflectance equivalent (V_{ROE}) methods are used in this thesis to compare maturities. The vitrinite reflectance scale for prediction of the hydrocarbon phase window for oil prone source rocks is 0-.6% (immature), .6-.9% (oil), .9-1.3% (wet gas), 1.3%+ (dry gas) (Senftle and Landis, 1991). There is not a single V_{ROE} estimate for each individual point in the adsorption data set, but there are many

V_{ROE} estimates throughout each wellbore containing the adsorption data points. I've averaged the V_{ROE} within each of the Marcellus members, Union Springs and Oatka Creek, for each well. This average should be representative for each formation member from which the adsorption sample points were obtained since the formation thickness does not exceed a few hundred feet. The vitrinite reflectance equivalence values give an estimate of thermal maturity in order to differentiate the adsorption data points from one another. The range of V_{ROE} of the sample points (Figure 6-2) is consistent with the high maturity shown in Figure 5-6. Just as the majority of the points in Figure 5-6 are of elevated maturity, the majority of the points plotted in Figure 6-2 are of thermal maturity greater than a V_{ROE} of 2. The three sample points of lowest maturity in Figure 5-6 equate to the points of lowest maturity in Figure 6-2.

X-Ray Diffraction

X-ray diffraction is used to determine mineralogy. The following description is summarized from Mason and Berry (1967). Samples are powdered and subjected to x-rays at varying angles of incidence to the sample. Final results of mineral and clay constituents are given in weight percents and volume percents. Volume percents can be calculated using density and porosity of the sample. Lu et al. (1995), Ross and Bustin (2009), and Schettler et al. (1991) all tested adsorption of methane on illite and found the mineral capable of adsorbing methane. For this reason I have collected x-ray mineralogy data to test whether there is any correlation of adsorption with clays or any other minerals.

Multiple Regression Analysis

While analyzing the data on Langmuir storage capacity (G_{SL}) in the Marcellus Shale, it became apparent that there are many factors that govern this property. In order to evaluate the strongest controls on G_{SL} , a multiple regression analysis in Microsoft Excel was completed. The output from Excel can be seen in Tables 7-1, 7-2, and 7-3 from different regression analyses completed in this paper. The adjusted R Square value shows the strength of the independent

variables that predict the value of the dependent variable. The closer this value is to 1, the greater the influence of the independent variables. The Significance F under the ANOVA table evaluates if the data is a good fit for the model. Values less than 0.05 are good fits. The Coefficients are used to calculate a predicted model for the dependent variable y. The coefficients have units that eliminate the units of the input variables to equal the units of the output. For example, if the equation is

$$y \text{ (} y \text{ units)} = x \text{ (} x \text{ units)} * \textit{Coefficient} \left(\frac{y \text{ units}}{x \text{ units}} \right),$$

the coefficient means for every 1x input, there is a coefficient y output. This relationship can then be summed with multiple x inputs of differing units to get a total y output. The coefficient units are always $\frac{y \text{ units}}{x \text{ units}}$. This cancels out the input x units to equal an output y. The P-value in the final table evaluates the strength of the coefficient: values less than 0.05 are strong and values greater than 0.05 are weak. Regression model equations are built on the platform of Equation 4, where Y is the modeled (dependent variable) output and X1 through Xn are the independent variable inputs.

$$Y = X0 + (X1 * X1 \textit{ Coefficient}) + (X2 * X2 \textit{ Coefficient}) + \dots + (Xn * Xn \textit{ Coefficient}) \dots \dots \dots (4)$$

This tool allows the user to evaluate the strength of any range of input variables in predicting an output value, and rank the weight of each independent variable on the output dependent variable.

Spotfire Analytics

The data will be analyzed using Tibco® Spotfire. This software will enable me to graph and compare multiple variables on one graph. Visualizing relationships within the data is essential to understanding the results and discovering why certain relationships exist.

Chapter 6

Results

Methane adsorption isotherms were measured on 34 samples of Marcellus shale of varying thermal maturity and mineralogy. Figures 6-1, 6-2, 6-3, 6-4 and 6-5 are the Langmuir storage capacity (G_{SL}), thermal maturity (V_{ROE}), TOC vol%, clay volume percent (vol%), and porosity percent (%) distributions, respectively, for the data set. As discussed earlier, all previous studies including methane adsorption isotherms found a positive linear correlation between adsorption volume and TOC content. This correlation can also be observed within the data set: increasing TOC vol% yields increasing storage capacity (Figure 6-6). In observing those four figures, it is evident that the anoxic depositional setting has the highest volumes of TOC and highest storage capacities compared to the dysoxic depositional setting.

With guidance from Gasparik et al. (2014), I've normalized adsorptive storage capacity to TOC vol% due to its dependence on organic matter. Figure 6-7 is the comparison of the Langmuir storage capacity (G_{SL}) normalized by TOC vol% vs. average thermal maturity (V_{ROE}). An increase in normalized G_{SL} volume occurs from thermal maturities of 1% to 1.7% V_{ROE} , flattens out to 2.2% V_{ROE} , and then decreases as maturity increases up to 4% V_{ROE} .

Figure 6-8 is a plot of porosity % vs. thermal maturity (V_{ROE}). As thermal maturity is increasing, porosity is decreasing at a logarithmic rate. Figure 6-9 is a plot of Langmuir Pressure (P_L) vs. thermal maturity (V_{ROE}). P_L remains relatively flat until a V_{ROE} of 2%, and then drops to remain relatively flat again as maturity increases to 4%. Figure 6-10 is a plot of thermal maturity (V_{ROE}) vs. deep resistivity (ohm*m). This plot shows resistivity decreasing as thermal maturity increases. Figure 6-11 is a plot of Langmuir storage capacity (G_{SL}) vs. clay volume %, showing a weak negative relationship of the volume of clay and the methane volume adsorbed. No other minerals had any constraining relationships on methane adsorption capacity. Micro-porosity is believed to be one of the controlling factors of sorbed gas volume (Heller and Zoback, 2014). Figure 6-12 is a plot of G_{SL} vs. porosity%. Samples with porosities lower than 10% show some positive correlation with adsorptive storage capacity, but once porosities exceed 10%, there is no

recognizable correlation. Figure 6-13 a plot of bulk density (g/cc) vs. porosity %. There is a negative linear trend of decreasing density as porosity is increasing. Figure 6-14 is a plot of bulk density (g/cc) vs. thermal maturity (V_{ROE}). This comparison yields a logarithmic trend of density increasing with increasing thermal maturity.

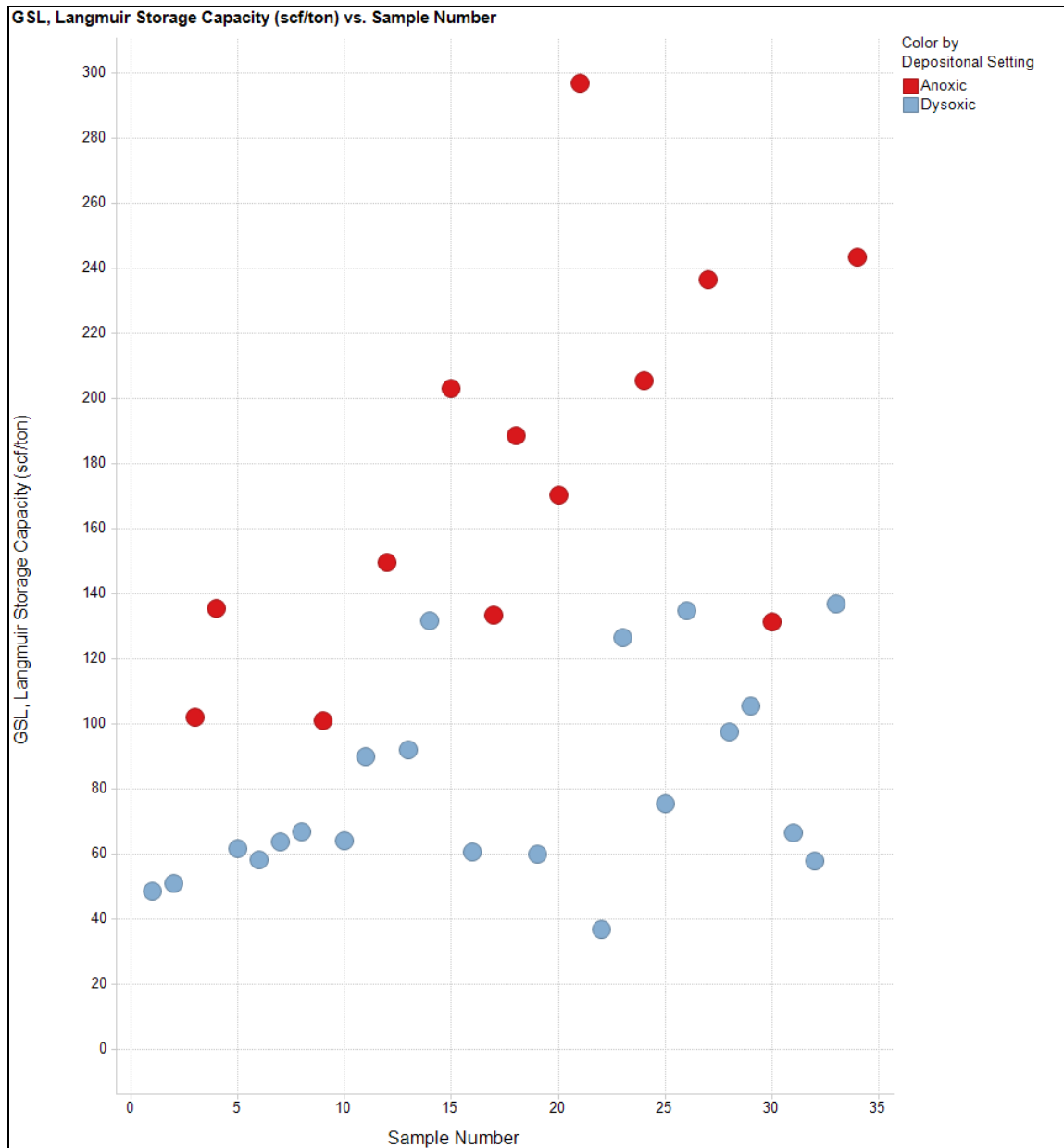


Figure 6-1 G_{SL} , Langmuir Storage Capacity (scf/ton) vs. Sample Number

The sample set includes a wide range of values for the storage capacity. Color coding is by depositional setting: Anoxic is red and dysoxic is blue. Samples deposited in an anoxic environment have higher Langmuir storage capacities than those in dysoxic environments.

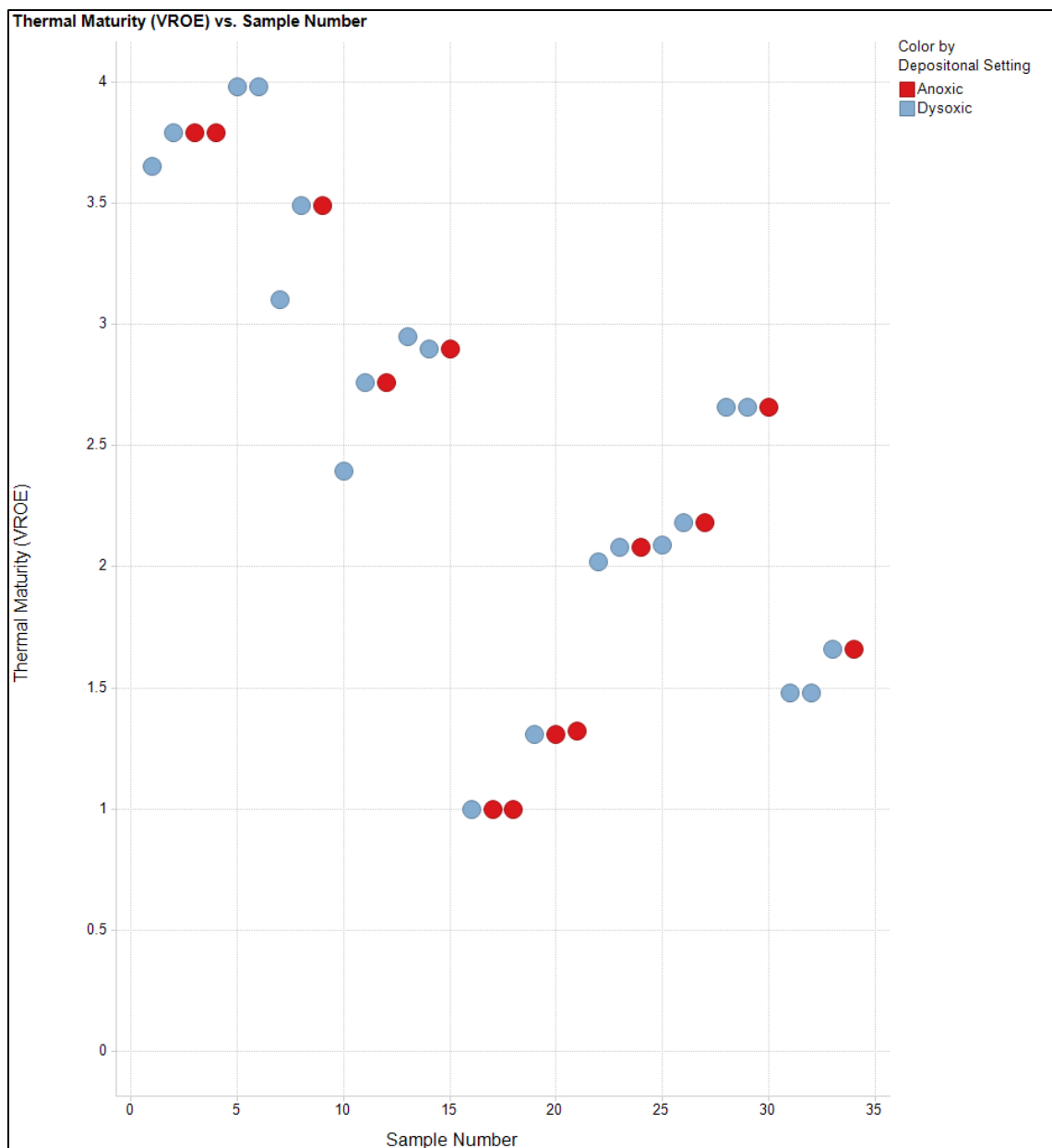


Figure 6-2 Thermal Maturity (V_{ROE}) vs. Sample Number

Vitrinite reflectance equivalent values vary from 1 to 3.9 for the data set with a relatively uniform spread of maturities. Color coding is by depositional setting: Anoxic is red and dysoxic is blue.

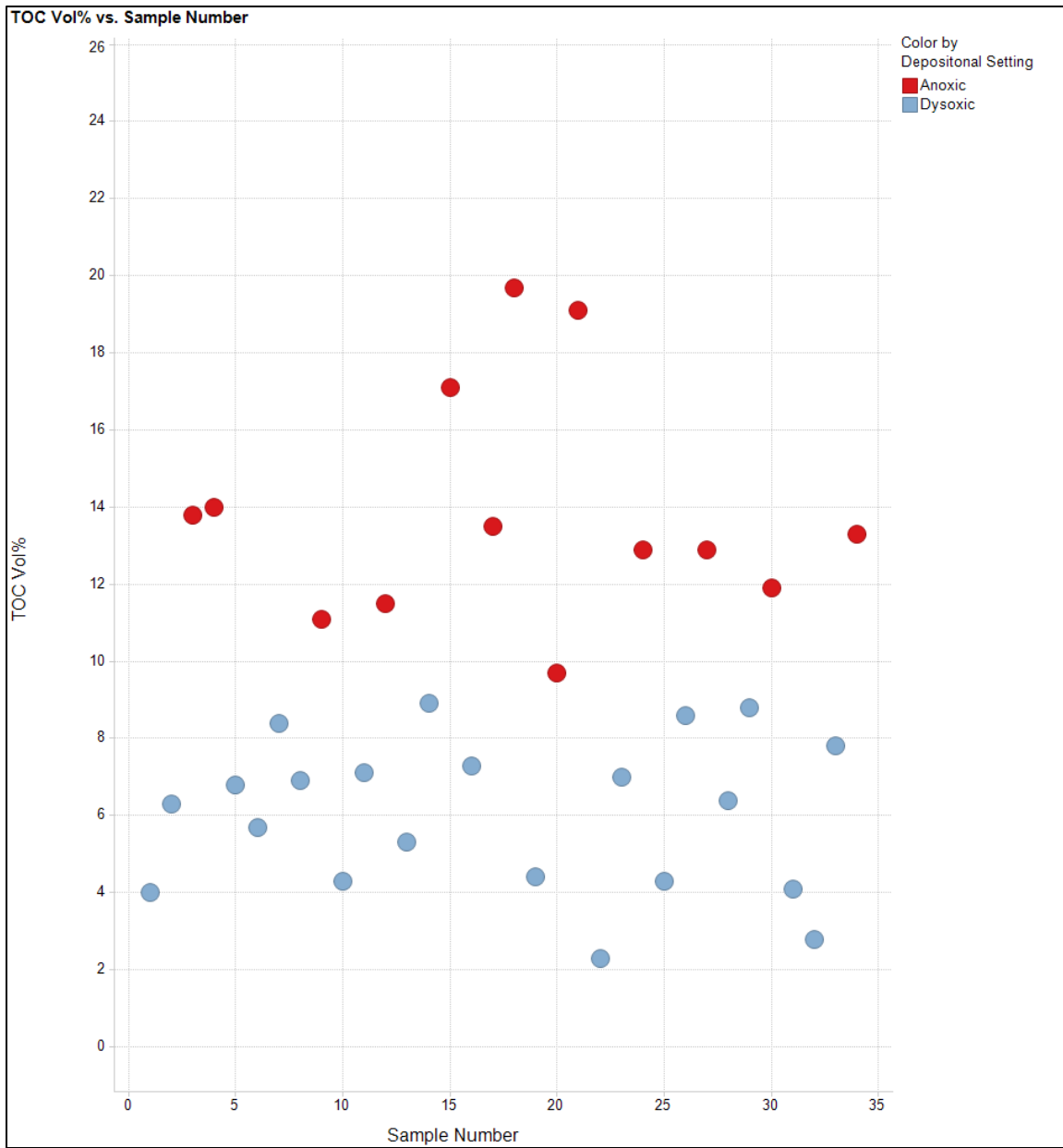


Figure 6-3 TOC vol% vs. Sample number

The anoxic samples have the highest TOC volumes while the dysoxic samples contain less TOC.

Color coding is by depositional setting: Anoxic is red and dysoxic is blue.

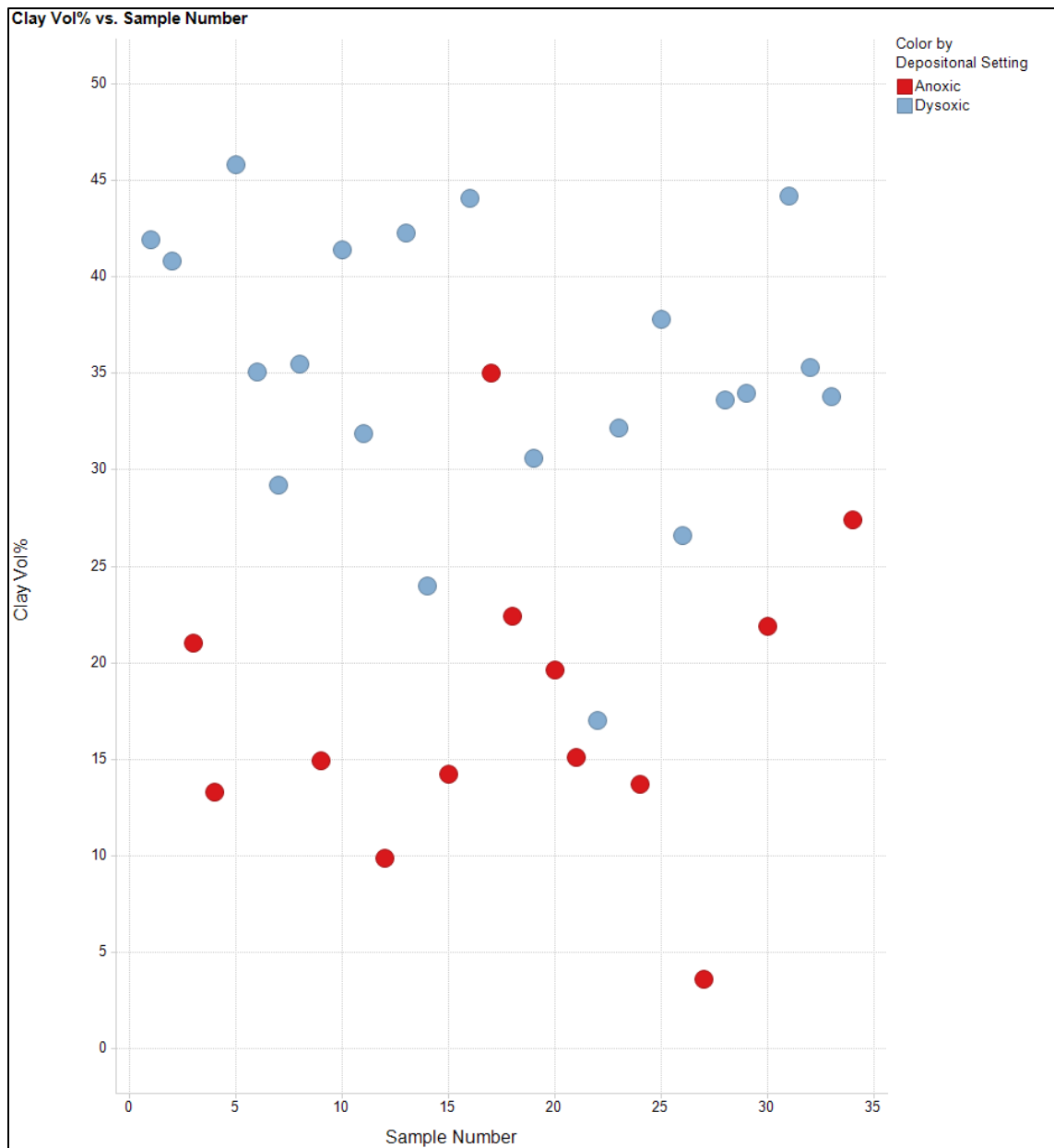


Figure 6-4 Clay vol% vs. Sample Number

Dysoxic samples tend to have higher volume percents of clay than anoxic samples do. Color coding is by depositional setting: Anoxic is red and dysoxic is blue.

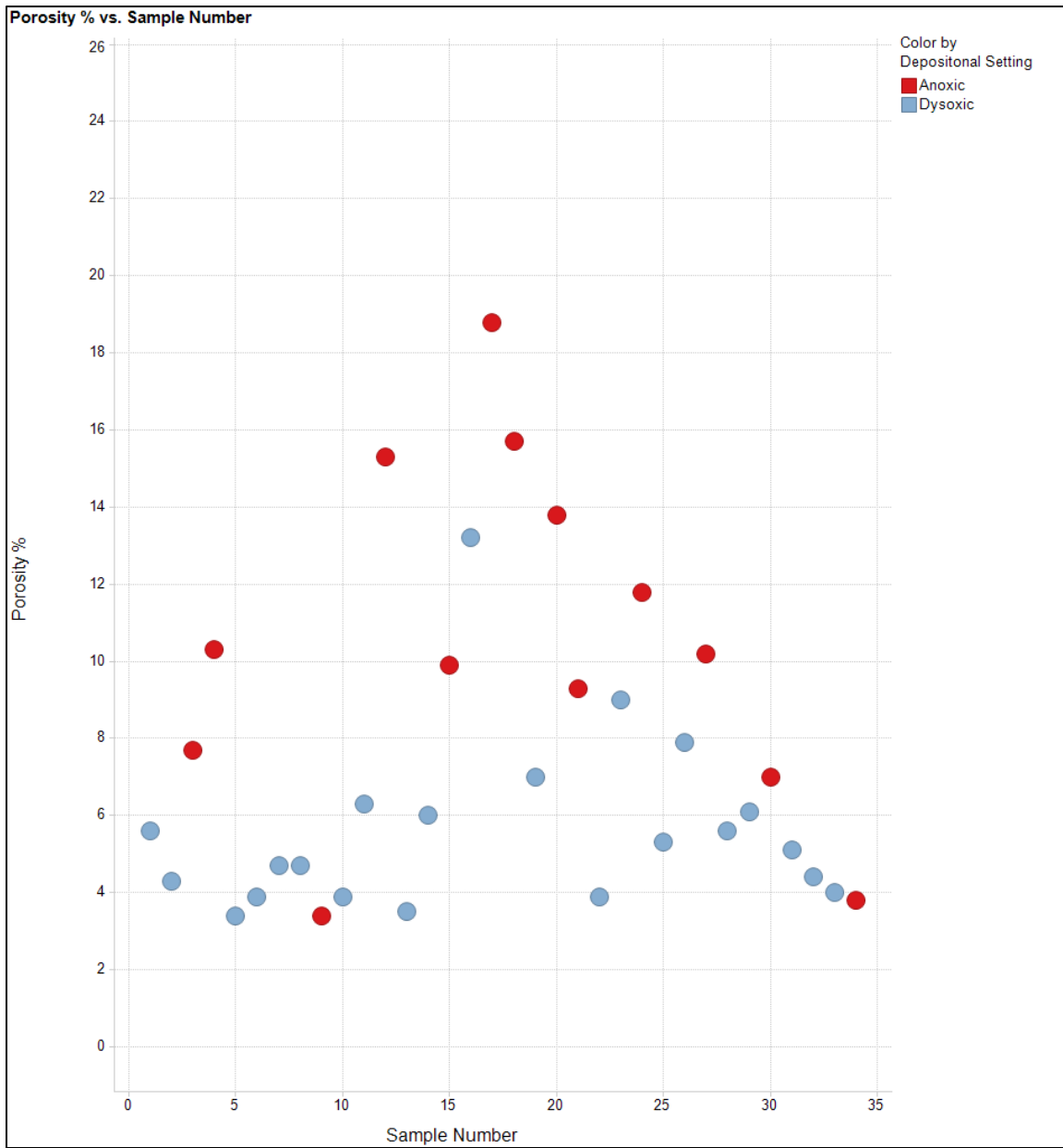


Figure 6-5 Porosity % vs. Sample Number

Samples that are anoxic generally have a higher porosity percent than dysoxic samples. Color coding is by depositional setting: Anoxic is red and dysoxic is blue.

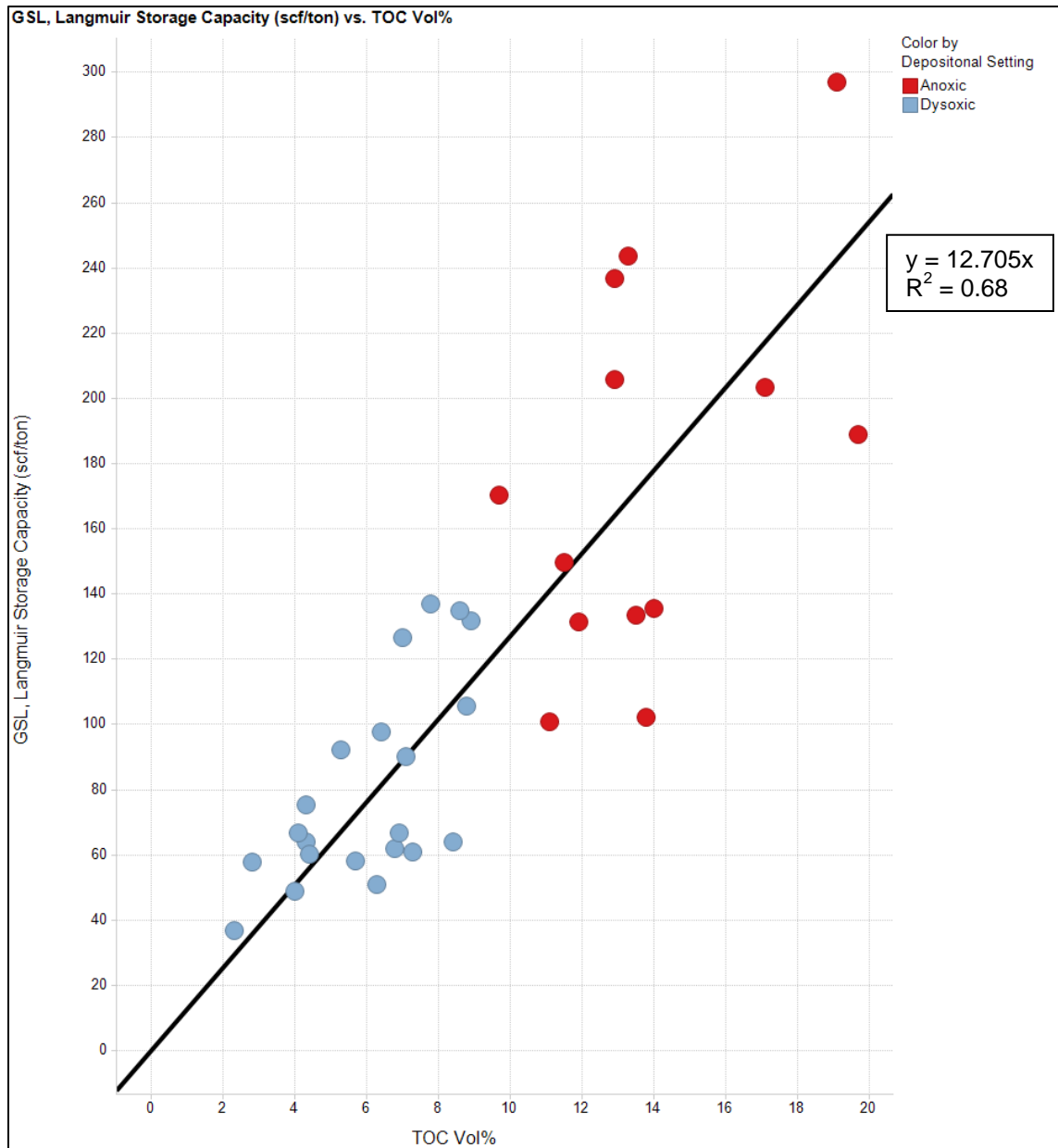


Figure 6-6 G_{SL} , Langmuir Storage Capacity (scf/ton) vs. TOC vol%

Color coding is by depositional setting: Anoxic is red and dysoxic is blue. The anoxic samples contain the highest volume of TOC and the highest Langmuir storage capacities. The dysoxic samples contain the lowest TOC and storage capacity volumes. The equation represents a positive linear relationship between G_{SL} and TOC vol% with a R^2 fit of 0.68.

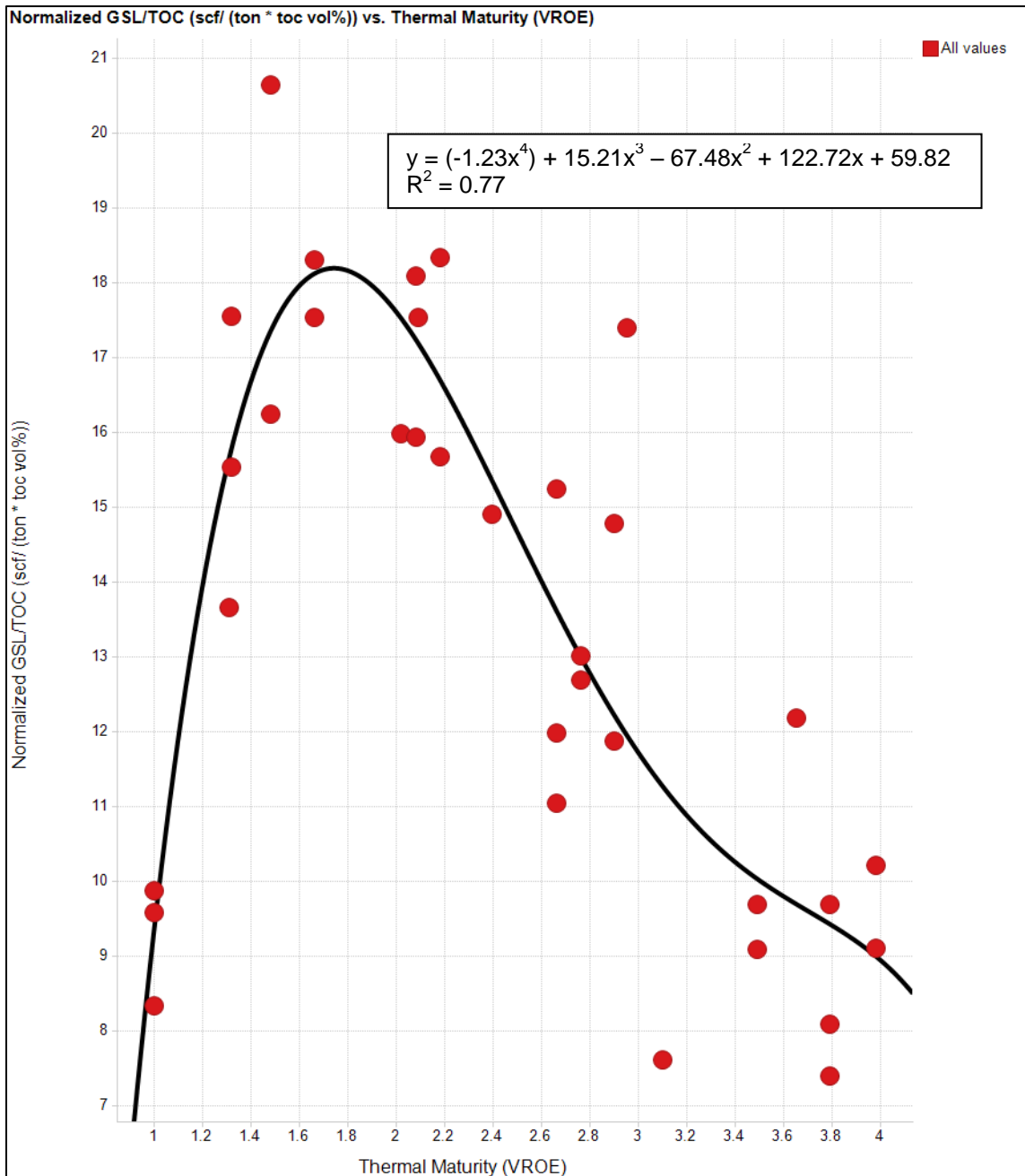


Figure 6-7 Normalized G_{SL} / TOC (scf/(ton*toc vol%)) vs. Thermal Maturity (V_{ROE})

Normalized adsorptive storage capacity increases for vitrinite reflectance equivalent values of 1% to 1.7% V_{ROE} , flattens out from 1.7% to 2.2% V_{ROE} , and then decreases as maturity increases up to 4% V_{ROE} . The data is fit with a 4th degree polynomial equation with an R^2 of 0.77.

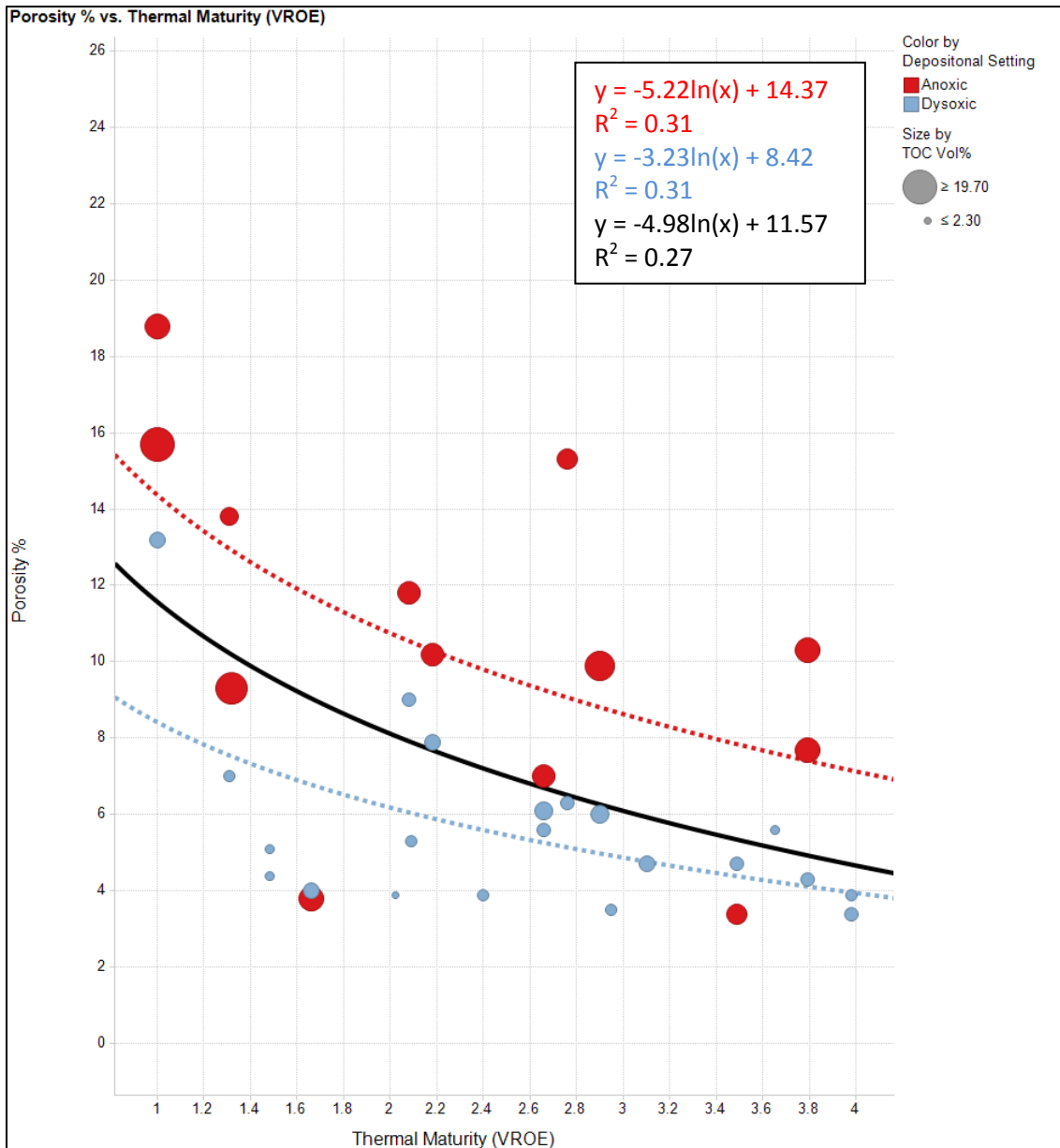


Figure 6-8 Porosity % vs. Thermal Maturity (V_{ROE})

As thermal maturity increases, porosity percent decreases. Color coding is by depositional setting: Anoxic is red and dysoxic is blue. Sizing of data is by TOC vol%. Anoxic samples with higher TOC vol% tend to have higher porosity than dysoxic samples with lower TOC vol%. The black line is the trend for all samples with an R^2 of 0.27. Colored curves are separated out by depositional setting with slightly stronger correlation R^2 values.

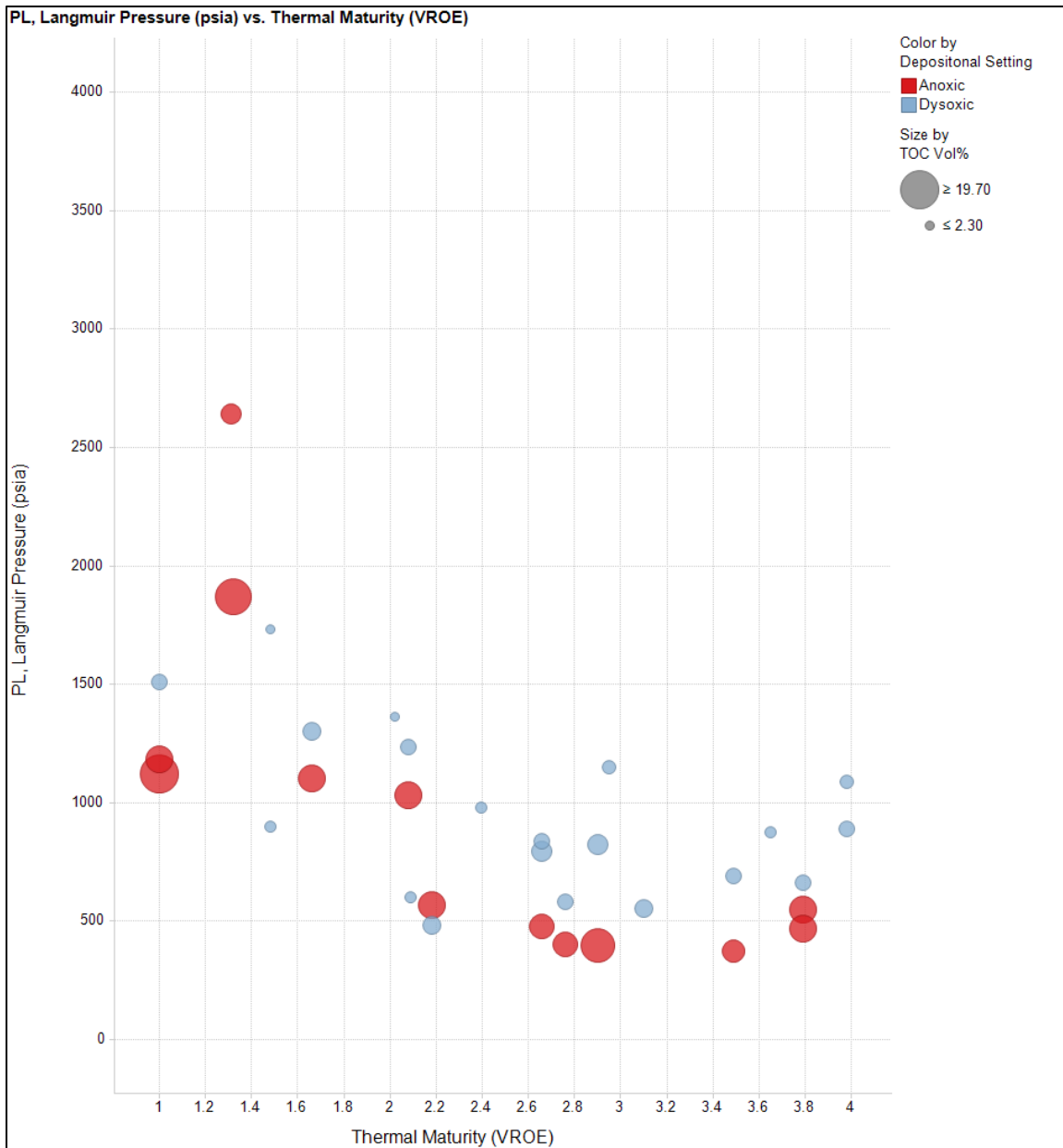


Figure 6-9 P_L , Langmuir Pressure (psia) vs. Thermal Maturity (V_{ROE})

P_L decreases for thermal maturities of 2.1% and greater compared to lower thermal maturities.

Color coding is by depositional setting: Anoxic is red and dysoxic is blue. The dysoxic samples fluctuate and don't follow the trend as well as the anoxic samples do.

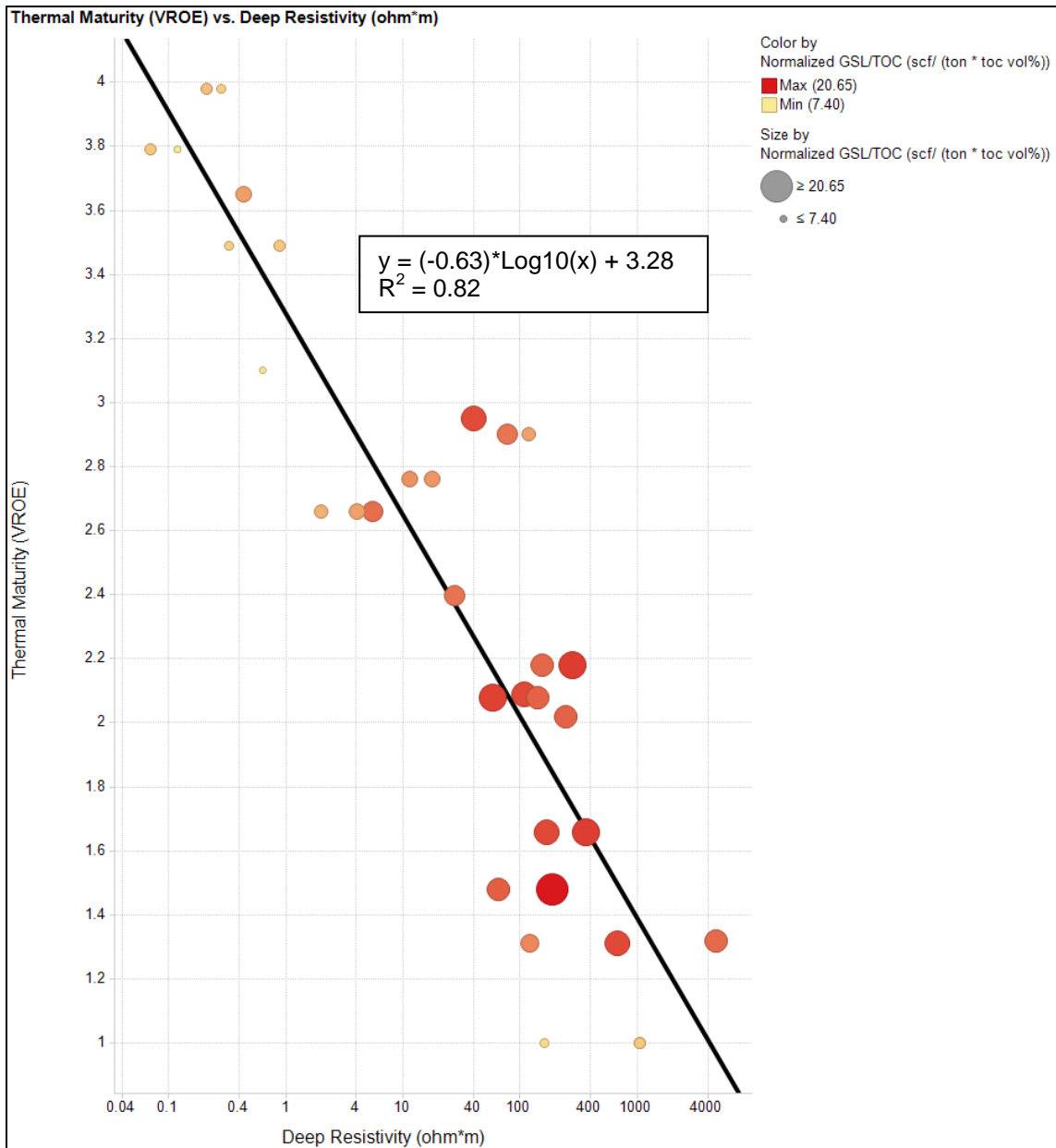


Figure 6-10 Thermal Maturity (V_{ROE}) vs. Deep Resistivity (ohm*m)

A decrease in resistivity indicates an increase in thermal maturity. Color is a gradient scale of normalized Langmuir adsorptive storage capacity G_{SL} / TOC , yellow being small volumes, red being large volumes. Size of dots is the same scale, smaller dots small volume, larger dots, larger volume. The data is best fit with a logarithmic curve with a R^2 value of 0.82.

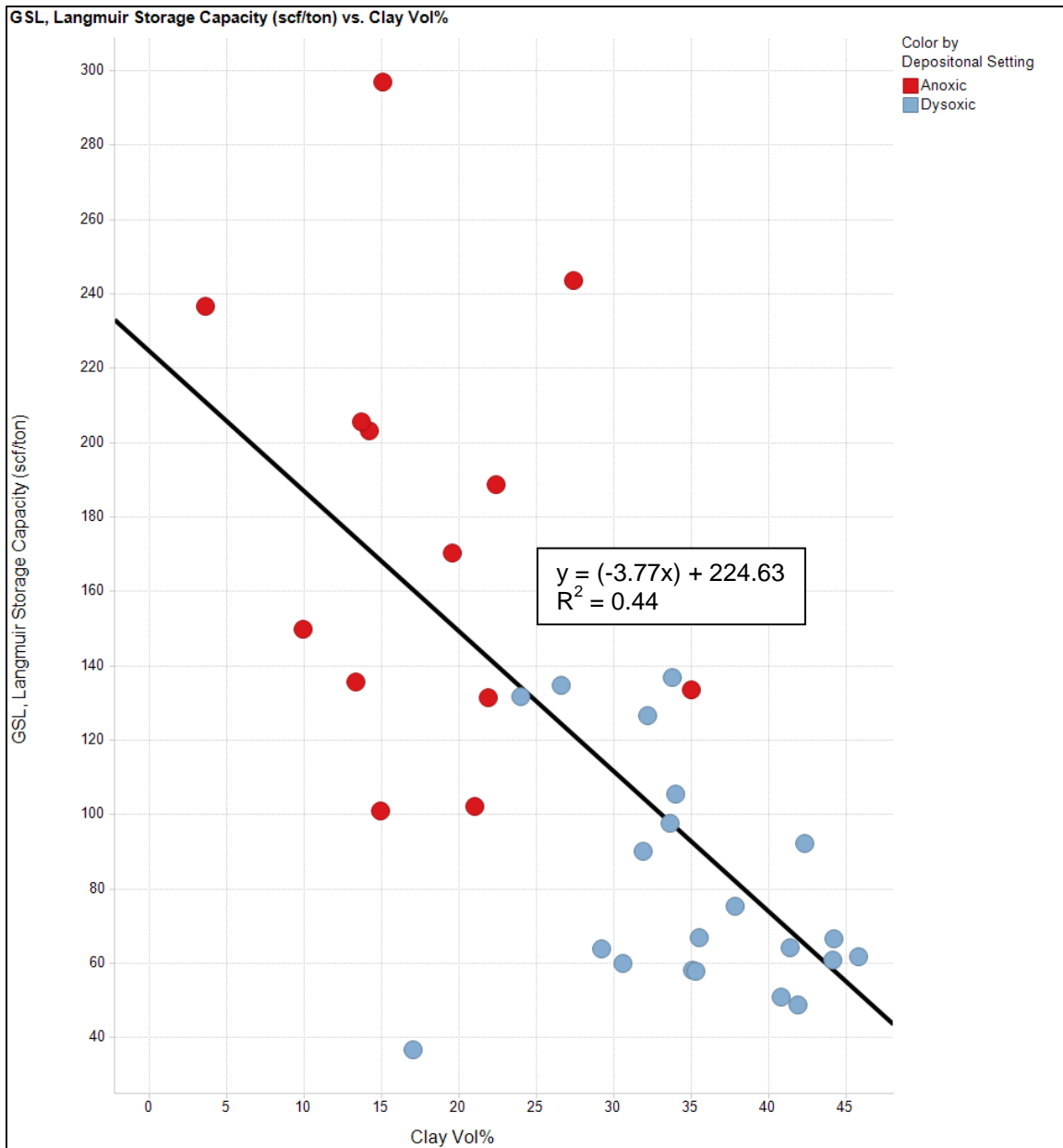


Figure 6-11 G_{SL} , Langmuir Storage Capacity (scf/ton) vs. Clay vol%

Color coding is by depositional setting: Anoxic is red and dysoxic is blue. The anoxic samples have the lowest clay contents and the highest storage capacities while the dysoxic samples have the highest clay contents and the lowest adsorptive storage capacities. The data is fit with a line of best fit with an R^2 of 0.44.

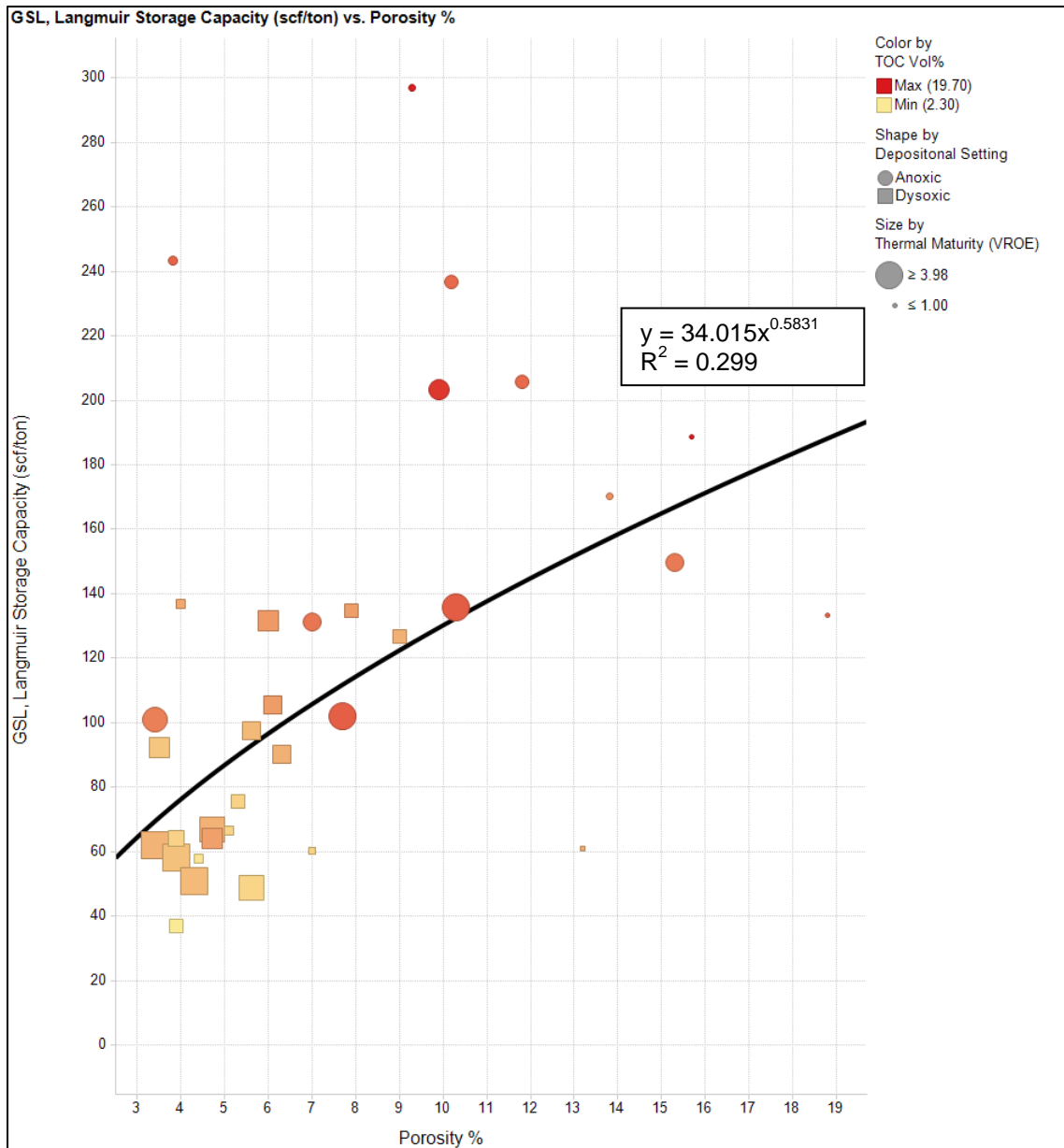


Figure 6-12 G_{SL} , Langmuir Storage Capacity (scf/ton) vs. Porosity %

Color grading is by TOC vol%. Red symbols have the highest TOC vol% and the yellow symbols have the lowest TOC vol%. Size is by thermal maturity (V_{ROE}), larger symbols have higher thermal maturity. Shapes are depositional setting: anoxic samples are circles and dysoxic samples are squares. The curve of fit is a power curve with an R^2 of 0.299.

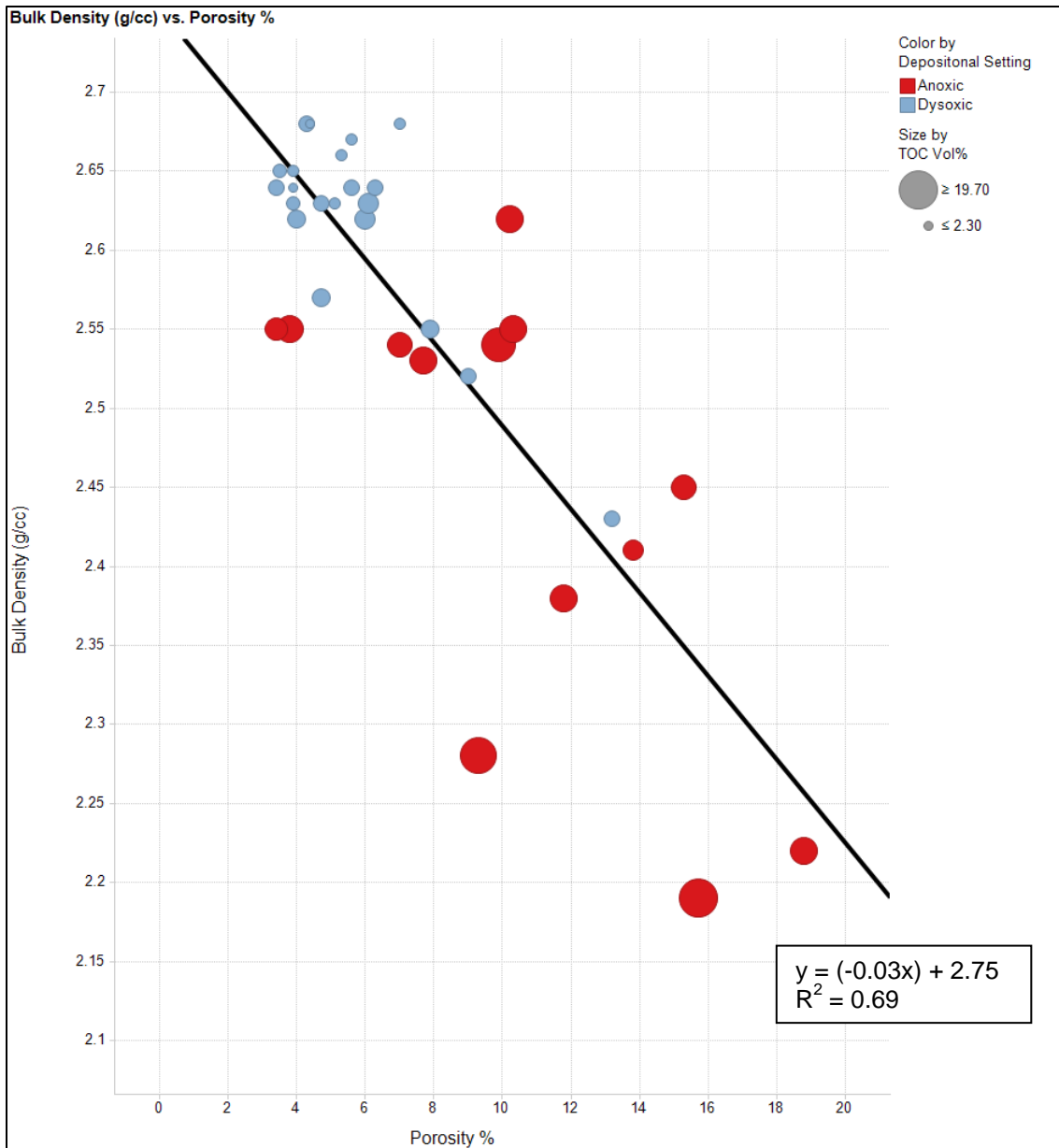


Figure 6-13 Bulk Density (g/cc) vs. Porosity %

Linear decrease in bulk density with the increase in porosity. Color coding is by depositional setting: Anoxic is red and dysoxic is blue. Sizing is by TOC volume percent (vol%), larger circles have higher TOC vol%. TOC vol% is decreasing as porosity decreases and bulk density increases. Samples of higher bulk density indicate potential compaction. The data is fit with a line of best fit with an R^2 of 0.69.

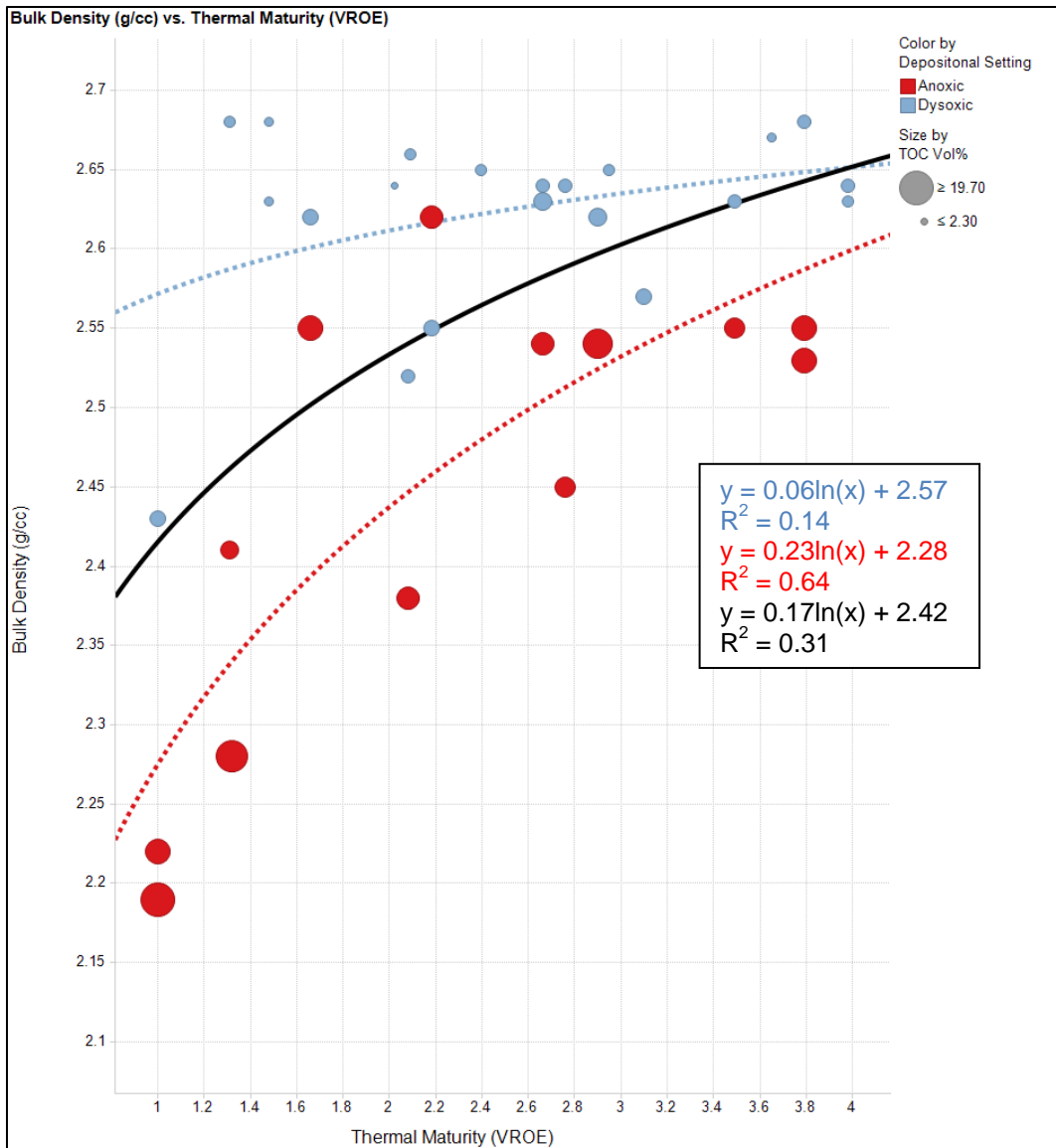


Figure 6-14 Bulk Density (g/cc) vs. Thermal Maturity (V_{ROE})

Color coding is by depositional setting: Anoxic is red and dysoxic is blue. Sizing is by TOC volume percent. As thermal maturity increases, sample bulk density also increases. Trends are broken up by depositional setting because of their TOC content. Samples with the highest TOC volumes (anoxic) will tend to have lower bulk densities. Curves are logarithmic trends of best fit. The black line is the trend for all samples with an R^2 of 0.31. Colored curves are separated out by depositional setting with stronger correlation R^2 values.

Chapter 7

Discussion and Interpretation

Many correlations were observed regarding methane adsorption, thermal maturity, and shale mineralogical content within the data set. The first correlation observed is the positive linear relationship between TOC vol% and Langmuir storage capacity (G_{SL} , scf/ton) (Figure 6-6). This relationship is in agreement with observations from Chareonsuppanimit et al. (2012), Gasparik et al. (2014), Guo (2013), Heller & Zoback (2014), Lu et al. (1995), Ross & Bustin (2009), Schettler et al. (1991), and Zhang et al. (2012) in their experiments of methane adsorption on organic gas shales. This relationship exists because the methane adsorbs onto the micro-pores of the organics in the shale, thus increased organics equals increased micro pore volume (Zhang et al., 2012; Heller & Zoback, 2014; Gasparik et al., 2014; Ross & Bustin, 2009; Ambrose et al., 2010).

The second observed correlation, one with perhaps a less obvious explanation, is the change in normalized adsorptive storage capacity with thermal maturity. I will discuss the plot (Figure 6-7) in two stages: thermal maturity of 1% to 1.8% V_{ROE} , and 2% to 4% V_{ROE} . From V_{ROE} 1% to 1.8%, normalized G_{SL}/TOC vol% increases. Schieber (2013) describes the development of organic porosity in Devonian shales with increasing thermal maturity beginning at percentages of .6%, and becoming well developed at maturities greater than 1.1% V_{ROE} . Schieber (2013) also describes continuous development of organic matter pores up to thermal maturities of 2% V_{ROE} . Figure 6-7 is in agreement with this observation: as thermal maturity increases from lower to higher maturities, adsorption volume increases in the presence of organic matter hosted pores.

As thermal maturity increases from 2% to 4% V_{ROE} , normalized G_{SL}/TOC vol% decreases. The decrease in adsorptive gas volume is probably due to a decrease in organic micro-pore porosity. Laughrey et al. (2011) describe a significant decrease in organic porosity in high maturity Marcellus samples (above 2% V_{ROE}). This loss in organic porosity is most likely due to the change in crystallography of organic carbon as it thermally matures. All carbonaceous material will move to its most stable forms of carbon when exposed to heat (Harrison 1979). For organic matter, the two most stable end points are methane and graphite. During metagenesis,

the final stage of thermal evolution, the remaining organic matter is completely depleted of its hydrogen (Horsfield and Rullkötter, 1994). It is during this stage where the remaining carbon forms stacked sheets of aromatic rings, the structure for graphite (Harrison, 1979). This is described by Harrison (1979) in a laboratory setting where organic material progressively transforms to graphite with increasing heat. In that experiment, graphite was detectable in samples that were heated to 300 degrees Celsius. In the northeast region of the Appalachian basin in Pennsylvania, near the depocenter of the basin, burial depths and burial temperatures reached 12km and 300 degrees Celsius, respectively (Beaumont et al., 1987). It is in this location where the adsorption sample points experience the highest thermal maturities. As organic material is progressively heated, the formation of graphite occurs due to a reduction of hydrogen. Due to graphite's nature to form condensed sheets, the size and connectivity of organic pores decreases. Although measurement of organic porosity would be difficult without the aid of scanning electron microscope (SEM) imagery, sample porosity is available and can be seen decreasing with increasing thermal maturity (V_{ROE}) in Figure 6-8. An extra level of compaction would have to occur to decrease the total rock volume, or else the decrease in organic volume would only increase total porosity of the rock. If further compaction did not occur, there would still be some decrease in adsorptive storage capacity because the internal surface area of the organic porosity is the main storage mechanism, which is lost with graphitization. Further SEM studies need to be conducted to confirm the decrease in total rock volume as well as a decrease in organic pore volume of over mature Marcellus.

Progressive transformation into stable end products of methane and graphite through thermal maturation yields higher maturity organic matter, which is less attractive to adsorbed methane than less mature organics. This decrease in affinity is a result of decreased sorption sites on organic matter for methane to condense onto. Stronger carbon to carbon bonds of graphite don't allow for weaker Van der Waals bonds of adsorbed methane to occur (Kwiecińska and Petersen, 2004). These phenomena in conjunction with previously stated decreases in

organic porosity are the two most likely explanations for decreased methane adsorption with increased maturity.

Langmuir pressure (P_L) vs. thermal maturity (V_{ROE}) in Figure 6-9 shows a higher P_L for samples of maturity less than 2% V_{ROE} compared to samples of higher maturity, greater than 2% V_{ROE} . P_L is the pressure at which $\frac{1}{2}$ of the Langmuir volume (G_{SL}) of gas has been adsorbed (Hartman 2012). Since there are less receptor sites for methane to adsorb in over mature rock with a decreased organic pore volume, the Langmuir volume of gas adsorbed will be less than in a rock with a higher organic pore volume, and the pressure at which $\frac{1}{2}$ the Langmuir volume is adsorbed will be lower too. This is the case for the Marcellus Formation.

During evaluation of the log data, it was observed that the higher the thermal maturity (V_{ROE}) of the well, the lower the resistivity. Figure 6-10 is a plot of thermal maturity (V_{ROE}) vs. deep resistivity. This trend suggests two things: increased conductivity and a decrease in hydrocarbons, often complimenting each other. The nature of graphite's structure allows it to be conductive (Kethireddy et al. 2014). Resistivity will decrease with increasing thermal maturity due to the progressive generation of graphite from the maturation and evolution of organic matter. Hydrocarbon presence can also increase resistivity. Decreases in resistivity with increased thermal maturity highlight the reservoir's decreasing ability to contain hydrocarbons. Dots on Figure 6-10 are color coded and size scaled to enhance the observation of increased adsorptive storage capacity at lower thermal maturities and higher resistivities, and the decrease of adsorptive storage capacity at higher thermal maturities and lower resistivities.

Figure 6-11 shows the negative relationship between clay mineral volume percent (vol%) and adsorbed Langmuir volumes (G_{SL}). The graph shows that the larger the clay mineral vol%, the smaller the G_{SL} . The data points on the graph are color coded by depositional setting. Coincidentally, the anoxic depositional setting, which has the highest TOC vol% (Figure 6-3) and has the highest Langmuir adsorption volumes, has the lowest clay volumes. Zhang et al. (2012) describes the effects of moisture on adsorption values, stating that moist samples will have lower adsorption volumes. This is due to clay's hydrophilic properties, and the possibility of in-situ

moisture blocking pore throats or adsorption sites on organic material (Zhang et al., 2012). The samples in the data set are tested as-received from core, and not dried, so samples with higher clay content could inhibit adsorption. Due to the negative relationship between clay vol% and TOC vol%, it is unclear if decreased adsorption is due to presence of moist clays, due to the absence of organic carbon, or a combination of both.

Figure 6-12 is a plot of Langmuir storage capacity (G_{SL}) vs. porosity percent. The colors represent a gradual change in TOC vol%, shapes highlight formation members, and size of the shapes increase with increasing thermal maturity (V_{ROE}). In the plot, as porosity decreases, G_{SL} and TOC vol% decrease. TOC vol% decrease is highlighted in a color change of red to yellow. Observing each shape category, sizes increase towards the origin. Pulling all the information together, this graph shows that samples with higher maturity experience a slight decrease in TOC vol%, a decrease in porosity %, and a decrease in G_{SL} .

Kinghorn and Rahman (1983) describe increases in kerogen's specific gravity with increases in thermal maturity. This observation can be seen in this data set through Figures 6-13 and 6-14. Figure 6-13 is a plot highlighting the relationship of an increasing sample bulk density with decreasing porosity. Figure 6-14 shows an increase in sample bulk density with an increase in maturity. The sample points are color coded by depositional setting due to the differences in TOC vol% between anoxic and dysoxic samples. Anoxic samples tend to have lower bulk densities compared to dysoxic samples. These two graphs, in conjunction with Figure 6-8 show that kerogen is losing its porosity and increasing in bulk density as it generates hydrocarbons and transforms to graphite with increasing thermal maturity.

The process of thermal maturation greatly alters organic shale's ability to be an adsorbent. As heating and maturation progresses, TOC decreases with the generation of hydrocarbons and organic bulk density increases. Induced stress decreases porosity, and in return, adsorption storage capacity decreases. Coincidentally, with a decrease in adsorbed gas, a reduction in resistivity can be observed as well. Analysis of this data set shows there are many controls on G_{SL} volumes in the Marcellus Formation. The first and most likely strongest control is

TOC vol%, which can be seen in Figure 6-6 as a positive linear trend between Langmuir adsorptive storage capacity (G_{SL}) and TOC vol%. The second is thermal maturity (V_{ROE}), which shows an increase then decrease in G_{SL}/TOC in Figure 6-7. The third is bulk density. With its strong correlation to porosity, increased porosities and decreased bulk densities result in increased G_{SL} 's, (Figures 6-8, 6-12, 6-13). Finally, in Figure 6-10, deep resistivity shows G_{SL} decreasing (bubble size) as resistivity decreases. Due to these multiple variables affecting the Langmuir storage capacity of the shale, a multiple regression analysis was conducted to evaluate the strength of each of the controls and investigate if Langmuir volume could be predicted using a regression model from these variables.

Multiple regression of G_{SL} was completed for the following variables: TOC vol%, thermal maturity (V_{ROE}), resistivity, and bulk density. Table 7-1 is the output from the regression analysis in Microsoft Excel. The adjusted R Square value of 0.91 means the input variables have a good correlation in predicting G_{SL} . The Significance F value of 2.64 E-18 means the data is a good fit for the model. Based off the P-values in the third table, the strength of the variables controlling Langmuir adsorption volumes are such from strongest to weakest: TOC vol%, bulk density, thermal maturity (V_{ROE}), and deep resistivity. The modeled Langmuir volume (G_{SLM}) can be calculated for each sample point by Equation 5.

Table 7-1 Multiple Regression Analysis statistics from G_{SLM}

<i>Regression Statistics</i>						
Multiple R	0.973338041					
R Square	0.947386942					
Adjusted R Square	0.908792303					
Standard Error	32.51948865					
Observations	34					
<i>ANOVA</i>						
	<i>df</i>	<i>SS</i>	<i>MS</i>	<i>F</i>	<i>Significance F</i>	
Regression	4	571271.4497	142817.8624	135.050163	2.64573E-18	
Residual	30	31725.51426	1057.517142			
Total	34	602996.964				
	<i>Coefficients</i>	<i>Standard Error</i>	<i>t Stat</i>	<i>P-value</i>	<i>Lower 95%</i>	<i>Upper 95%</i>
Intercept	0	#N/A	#N/A	#N/A	#N/A	#N/A
TOC Vol%	10.61615982	1.387709685	7.650130232	1.56234E-08	7.782078559	13.45024108
Thermal Maturity V _{ROE}	-15.55135002	6.923731681	-2.246093687	0.032216107	-29.69149648	-1.411203561
Deep Resistivity (ohmm)	0.010778024	0.008660711	1.244473403	0.222960468	-0.006909507	0.028465555
Bulk Density (g/cc)	22.12908668	7.964493288	2.778467616	0.009330973	5.863421467	38.3947519

$$\begin{aligned}
& \text{Modeled Langmuir volume } (G_{SLM}, \text{ scf/ton}) \\
& = (\text{TOC vol}\% * 10.62) + (\text{thermal maturity } (V_{ROE}) * (-15.55)) \\
& + (\text{deep resistivity (ohmm)} * 0.01) + (\text{bulk density } (\frac{g}{cc}) * 22.13) \\
& \dots\dots\dots(5)
\end{aligned}$$

Figure 7-1 is a representation of this output of measured Langmuir Volume (G_{SL}) vs. modeled Langmuir volume (G_{SLM}). The R^2 of this plot is 0.77 with a line of best fit equation $y=x$. I believe that this is a strong correlation of G_{SL} vs. G_{SLM} and propose the use of Equation 5 to predict Langmuir adsorption volumes in the absence of measured Langmuir data. If no core data is available, G_{SL} can be modeled solely with well logs and public thermal maturity data. First, TOC vol% needs to be modeled in the absence of core data.

Emery and Zagorski (2013) show a multiple regression of uranium (ppm) and bulk density to model TOC vol%. If a spectral gamma ray log is not available to obtain uranium ppm, uranium (ppm) can be estimated from its relationship with the gamma ray log (Figure 7-2). Spectral gamma ray logs were available for most of the wells in this data set so uranium (ppm) was used in this paper. Table 7-2 shows the multiple regression results for modeling TOC vol%. The adjusted R square value of 0.886 means the variables are a strong predictor for TOC vol%. A Significance F value of 6.38 E-13 supports the high R square value for the variables and their strength to predict TOC vol%. Each variable's P-value is less than 0.05 which means they both have a strong influence on the prediction of TOC vol% with uranium (ppm) being a stronger control than bulk density due to its smaller P-value. Equation 6 is the resulting equation from the regression used to predict TOC vol% at each sample point.

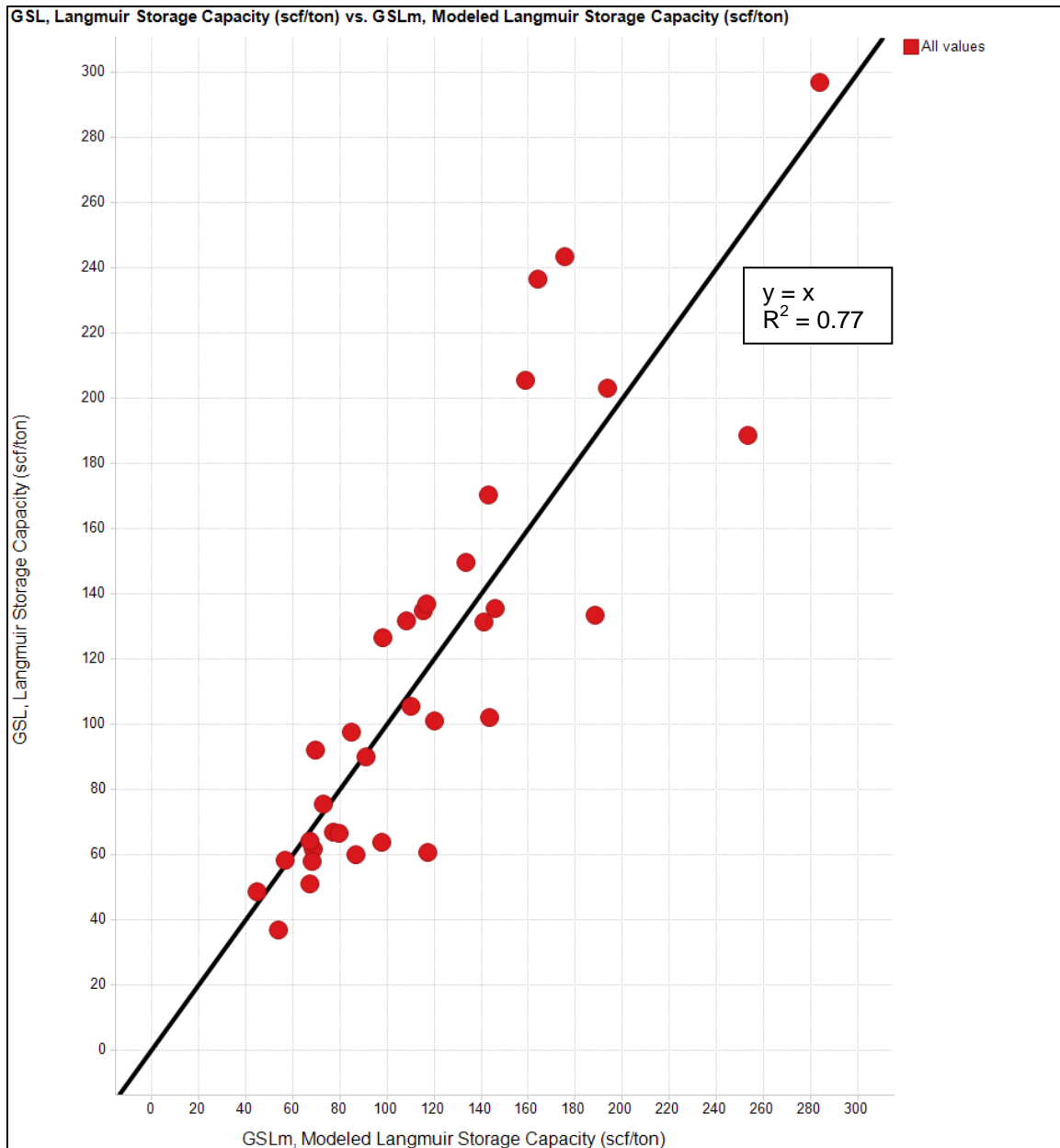


Figure 7-1 G_{SL} , Langmuir Storage Capacity (scf/ton) vs. G_{SLM} , Modeled Langmuir Storage Capacity (scf/ton)

The line of best fit is a 1:1 correlation with an R^2 of 0.77, meaning 77% of the data is explained by the line $y=x$. This regression can be used with the four factors controlling Langmuir storage capacity to predict its volume without the need for physical Langmuir adsorption data.

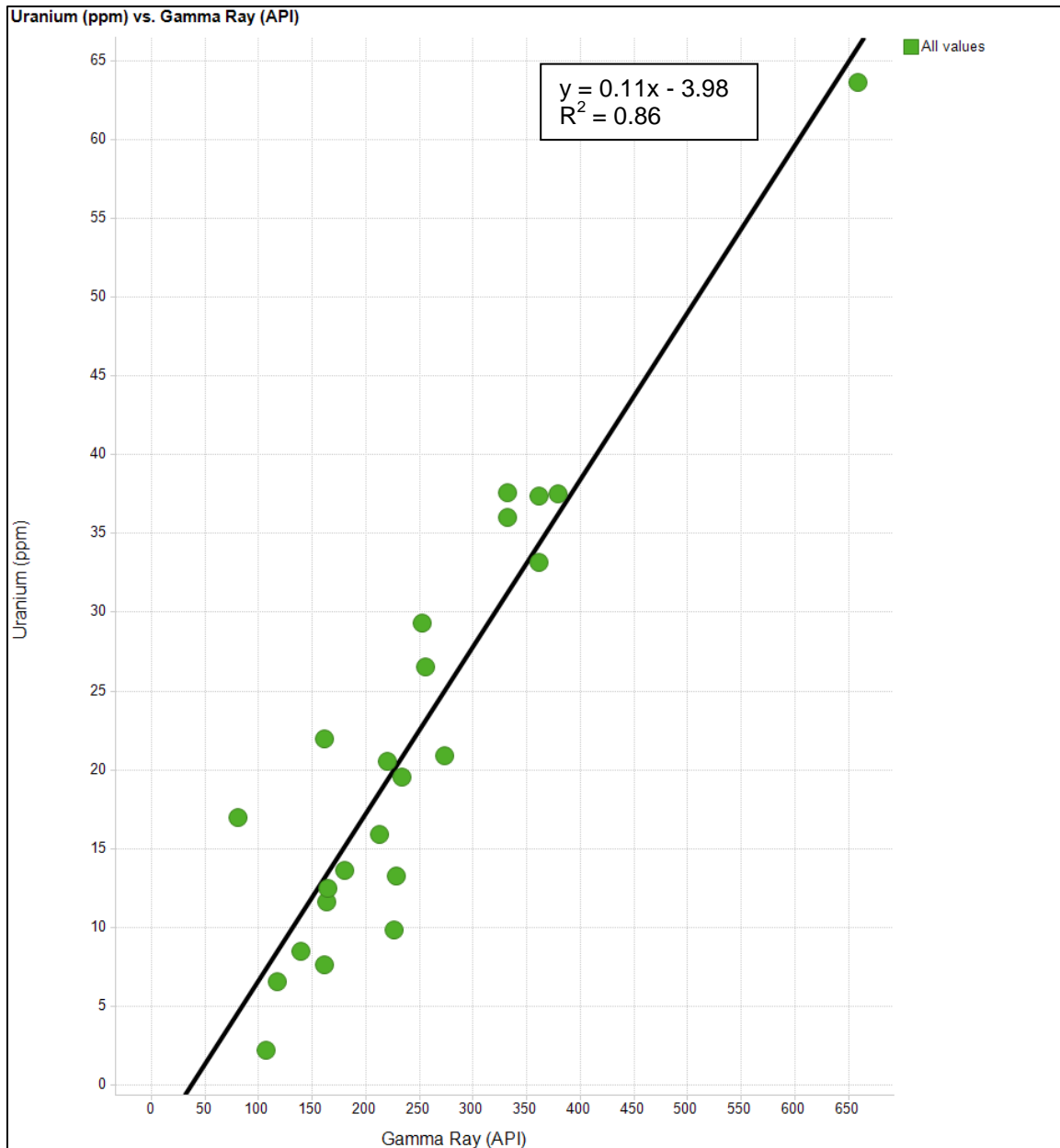


Figure 7-2 Uranium (ppm) vs. Gamma Ray (API)

This linear relationship highlights that 86% of the gamma ray signature is derived from uranium.

This relationship could be used to estimate uranium content if a spectral gamma ray is not available.

Table 7-2 Multiple Regression Analysis statistics from TOC_M

<i>Regression Statistics</i>						
Multiple R	0.967910291					
R Square	0.936850331					
Adjusted R Square	0.886224157					
Standard Error	2.822197204					
Observations	23					
ANOVA						
	<i>df</i>	<i>SS</i>	<i>MS</i>	<i>F</i>	<i>Significance F</i>	
Regression	2	2481.379262	1240.689631	155.7716564	6.38112E-13	
Residual	21	167.2607382	7.964797058			
Total	23	2648.64				
	<i>Coefficients</i>	<i>Standard Error</i>	<i>t Stat</i>	<i>P-value</i>	<i>Lower 95%</i>	<i>Upper 95%</i>
Intercept	0	#N/A	#N/A	#N/A	#N/A	#N/A
Bulk Density (g/cc)	1.102826096	0.408091732	2.702397546	0.013338778	0.254152883	1.951499309
Uranium (ppm)	0.30704312	0.040081804	7.660411674	1.63901E-07	0.223688446	0.390397794

$$\begin{aligned}
 & \text{Modeled TOC vol\% } (TOC_M) \\
 & = (\text{uranium (ppm)} * 0.31) + (\text{bulk density } (\frac{g}{cc}) * 1.10) \\
 & \dots\dots\dots(6)
 \end{aligned}$$

Figure 7-3 is the graph comparing the measured TOC vol% from core points vs. the modeled TOC_M vol% from uranium and bulk density. The R² of the comparison is 0.69, which means 69% of the data can be explained by the line of best fit y = x. This strong correlation allows me to use the modeled TOC vol% and re-run the modeling of G_{SL} using only log data.

A multiple regression was run using the same variables as was previously done with core TOC vol% but this time with all log data to model G_{SL}. These variables were: TOC_M vol%, thermal maturity (V_{ROE}), deep resistivity (ohm*m), and bulk density (g/cc). Table 7-3 shows the results with an adjusted R square value of 0.88 and significance value of 3.4 E-11, both supporting a strong model. Based off the P-values, the order of strongest to weakest variables influencing the calculation of modeled G_{SL} is: TOC_M vol%, deep resistivity (ohm*m), bulk density (g/cc), and thermal maturity (V_{ROE}). Equation 7 is the equation used to model Langmuir volume (G_{SLM}):

$$\begin{aligned}
 & \text{Modeled Langmuir volume } (G_{SLM}, \text{scf/ton}) \\
 & = (TOC_M \text{ vol\%} * 8.93) + (\text{thermal maturity } (V_{ROE}) * (-3.42)) \\
 & + (\text{deep resistivity (ohmm)} * 0.03) + (\text{bulk density } (\frac{g}{cc}) * 11.24) \\
 & \dots\dots\dots(7)
 \end{aligned}$$

Figure 7-4 is the comparison of Langmuir volume (G_{SL}) values measured from core vs. modeled Langmuir volume (G_{SLM}) from well logs. The line of best fit is y = x with an R² of 0.76. The log modeled G_{SL} has a good fit compared to the core measurements, and has a 0.01 lower R² fit to the core data than modeled G_{SL} using core TOC vol% values. Thus, using this proposed method of estimating G_{SL} from well logs (Equation 7) should be sufficient without the need of core data.

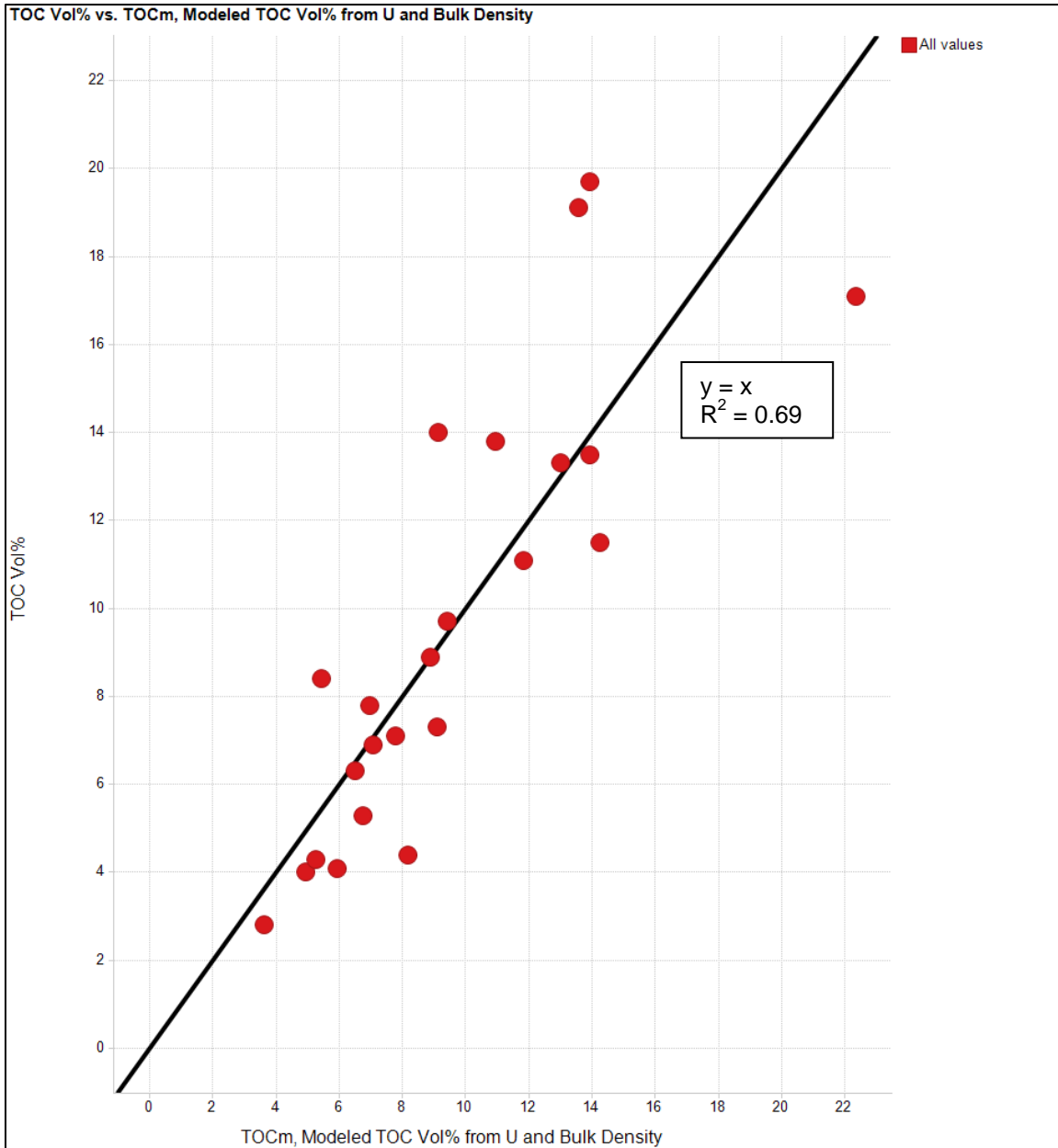


Figure 7-3 TOC vol% vs. TOC_M, Modeled TOC vol% from U and Bulk Density

This 1:1 relationship shows that TOC vol% can effectively be modeled from these two logs and that 69% of the data is explained by the $y=x$ relationship.

Table 7-3 Multiple Regression Analysis statistics from G_{SLM} using all logs

<i>Regression Statistics</i>						
Multiple R	0.971441496					
R Square	0.943698581					
Adjusted R Square	0.882177304					
Standard Error	35.20372466					
Observations	23					
ANOVA						
	<i>df</i>	<i>SS</i>	<i>MS</i>	<i>F</i>	<i>Significance F</i>	
Regression	4	394679.7041	98669.92603	79.61732306	3.41597E-11	
Residual	19	23546.74237	1239.30223			
Total	23	418226.4465				
	<i>Coefficients</i>	<i>Standard Error</i>	<i>t Stat</i>	<i>P-value</i>	<i>Lower 95%</i>	<i>Upper 95%</i>
Intercept	0	#N/A	#N/A	#N/A	#N/A	#N/A
Thermal Maturity V_{ROE}	-3.424370391	8.31738675	-0.411712295	0.685157709	-20.83286089	13.98412011
Deep Resistivity (ohmm)	0.033352845	0.008576348	3.88893326	0.000987456	0.015402342	0.051303348
Bulk Density (g/cc)	11.23955377	10.48538475	1.071925737	0.297180788	-10.70660868	33.18571622
TOC _M	8.933212144	1.753254422	5.095217233	6.42996E-05	5.263608473	12.60281581

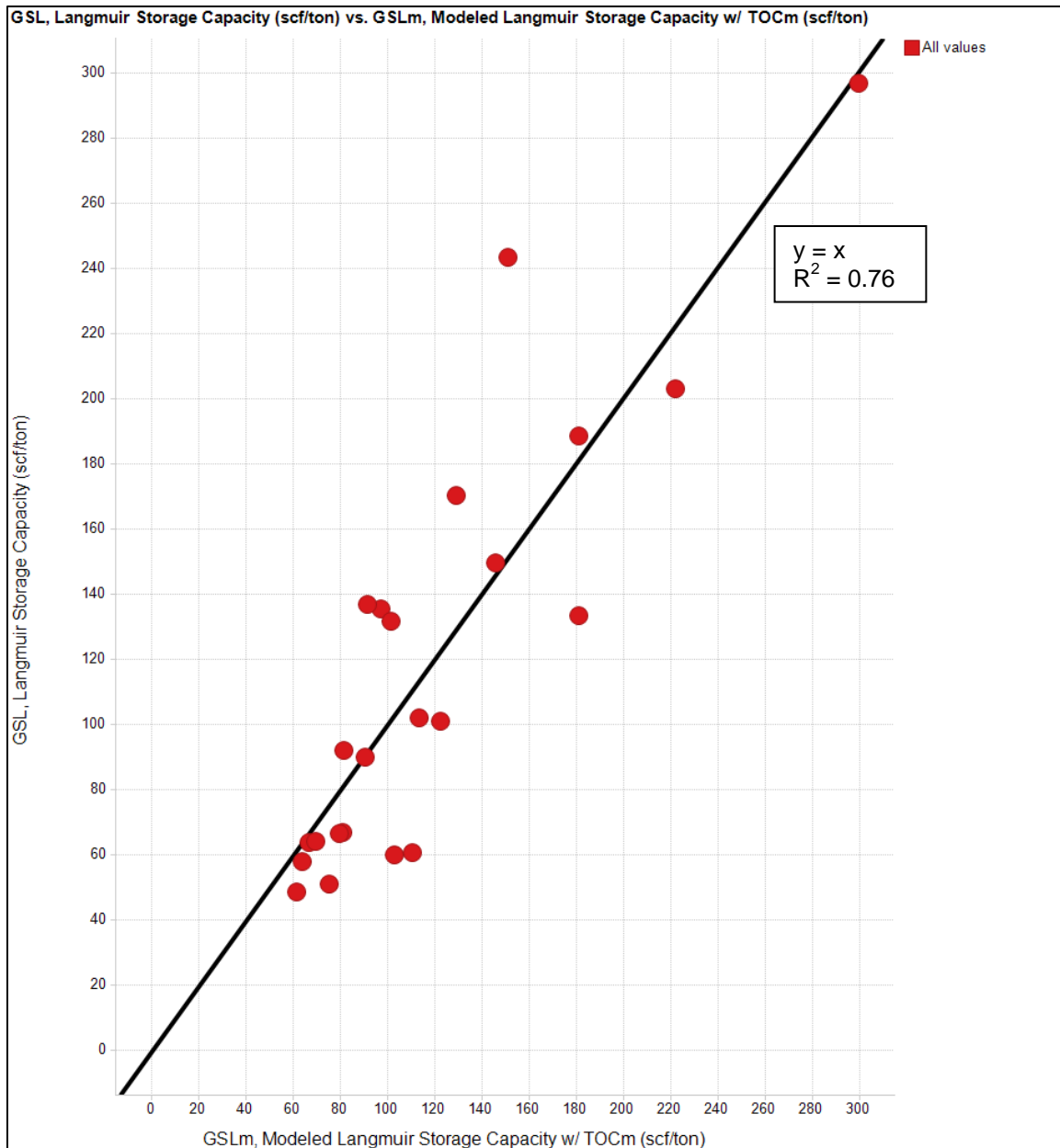


Figure 7-4 G_{SL} , Langmuir Storage Capacity (scf/ton) vs. G_{SLM} Modeled Langmuir Storage Capacity with TOC_M (scf/ton)

The line of best fit is a 1:1 correlation with an R^2 of 0.76, meaning 76% of the data is explained by the line $y=x$. This regression can be used with the four factors controlling Langmuir storage capacity as log data to predict its volume without the need for physical Langmuir adsorption data.

Using this method to model G_{SL} , a geologist can take these equations, and apply them to the entire Marcellus Formation and get estimates for G_{SL} throughout the wellbore. Instead of sampling a few select core points, the entire well can be estimated at depth increments of 0.5 ft (or the best resolution of available logs). Figure 7-5 is a plot of the two original type logs with the 4th track representing the results from the modeled work. First, the original core sample points are plotted as dots. Green circles are TOC vol% from core and black squares are G_{SL} (scf/ton) from core. The black curve is modeled TOC vol% from logs (TOC_M vol %). The red curve and fill is the modeled Langmuir volume (G_{SLM} scf/ton) from log data. The black dashed line is the thermal maturity (V_{ROE}). From this modeled Langmuir volume (G_{SLM}), if a relationship between G_{SL} and free gas could be established, total gas-in-place could be estimated throughout the wellbore, then on a basin-wide scale, enabling the user to highlight areas of higher gas-in-place, and potentially greater productivity.

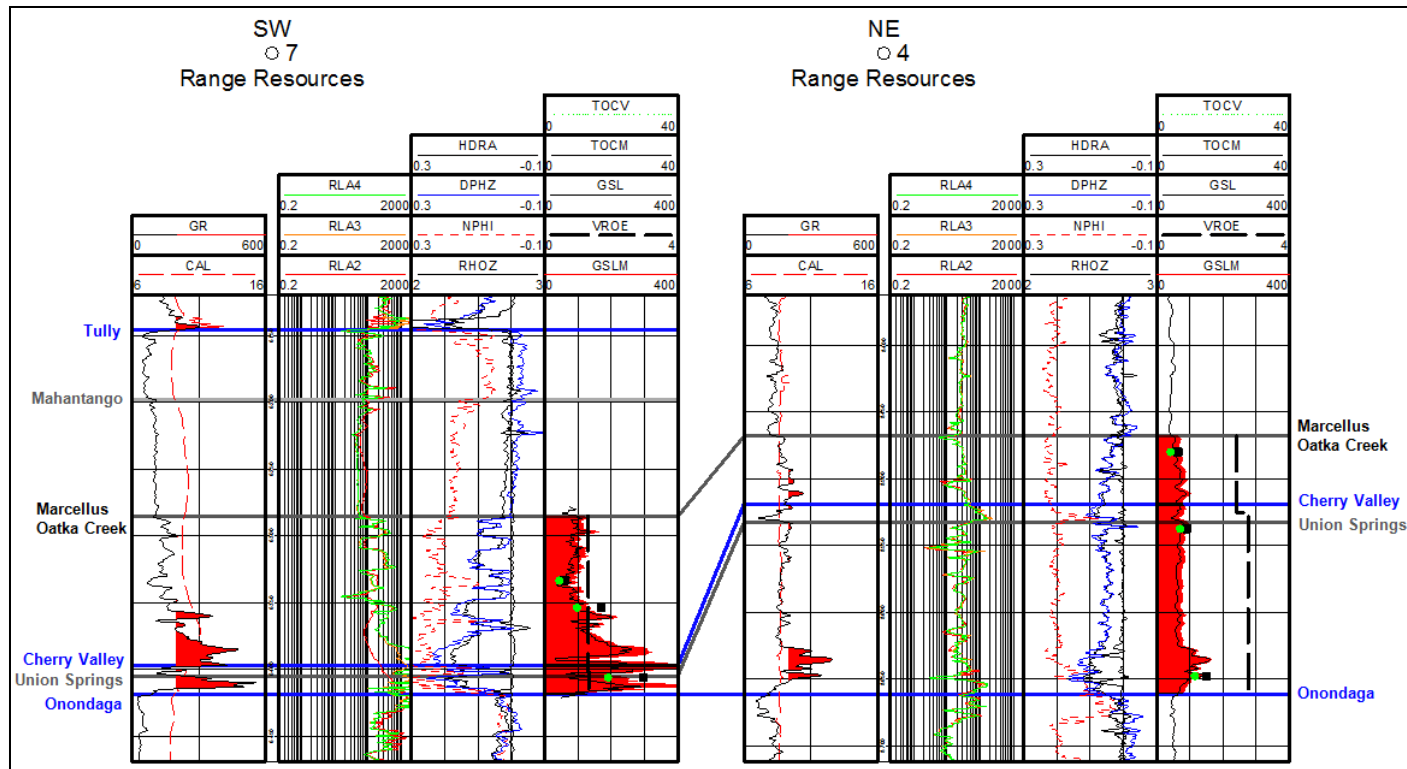


Figure 7-5 Type logs of Marcellus Formation from core production areas with TOC_M and G_{SLM} curves plotted

Green circles are TOC vol% from core and black squares are G_{SL} (scf/ton) from core. The black curve is modeled TOC vol% from logs (TOC_M vol %). The red curve and fill is the modeled Langmuir volume (G_{SLM} scf/ton) from log data. The black dashed line is the thermal maturity (V_{ROE}). This plot shows that G_{SL} can be modeled for the entire wellbore as opposed to the three selective core points. This allows the geologist to more effectively evaluate gas storage potential on a full well basis.

Chapter 8

Conclusions

This study evaluated methane storage capacity and its relationship with thermal maturity in the Middle Devonian organic rich Marcellus Shale using core and log data. Through the use of direct comparison, many rock properties, including thermal maturity, were found to be influences on Langmuir methane storage capacity.

1. TOC vol% and Langmuir methane adsorption storage capacity (G_{SL}) have a positive linear relationship.
2. Langmuir methane adsorption storage capacity (G_{SL}) was normalized by TOC vol% to eliminate potential of miss-interpreting gas volumes due to large TOC volumes.
3. Normalized $G_{SL}/\text{TOC vol\%}$ increases with thermal maturity (V_{ROE}) until approximately 2% V_{ROE} .
4. $G_{SL}/\text{TOC vol\%}$ decreases as thermal maturity increases to 4% V_{ROE} .

Once there was a realization that normalized adsorptive storage capacities change over a spectrum of thermal maturities, changes in rock properties were highlighted in comparison to thermal maturity.

5. A decrease in porosity occurs with increasing thermal maturity (V_{ROE}).
6. A decrease in Langmuir pressure (PL) occurs for thermal maturities greater than 2% V_{ROE} .
7. Deep resistivity decreases with increasing thermal maturity (V_{ROE}).

Other comparisons to Langmuir storage capacity were made to try to understand factors that affected the property.

8. There is a negative relationship between clay volumes and Langmuir storage capacity
9. There is a positive correlation of porosity % and Langmuir methane adsorption (GSL).

Finally, explanations were given as to why G_{SL} behaved the way it did over an increasing spectrum of thermal maturities

10. The decrease in normalized adsorptive storage capacity with increasing thermal maturity greater than 2% VROE is explained by a decrease in organic porosity, the primary host for adsorbed methane, as a result of changes in organic carbon crystallography.

11. There is a decrease in affinity between adsorbed methane and organic carbon due to the change in crystallography of organic carbon.

It is clear that there are many factors affecting the Langmuir storage capacity (G_{SL}) of adsorbed methane in the Marcellus shale. First using core and well logs, G_{SL} was modeled at for the depths samples. Then, using only well logs, G_{SL} was successfully modeled for the entire wellbore of 2 type logs.

12. Using multiple regression analysis, the four strongest factors governing methane adsorption: TOC vol%, bulk density, thermal maturity, and deep resistivity, were compared against Langmuir volume (G_{SL}), and a correlation was observed.

13. TOC vol% was then modeled from a multiple regression of uranium and bulk density from wireline logs to eliminate need for core values.

14. The new modeled TOC vol% was used in a new multiple regression of G_{SL} using the original variables and the strong relationship was upheld.

15. Using only well logs, G_{SL} was modeled for the entire wellbore enabling G_{SL} to be estimated at many depths as opposed to the previous selective core points.

With a strong correlation between modeled G_{SL} and measured G_{SL} , the relationship between G_{SL} and its four factors could be used to model and predict G_{SL} in areas where adsorption data is un-available. Using modeled G_{SL} data and its relation to free gas volumes, gas-in-place could be estimated on a basin-wide scale using publicly accessible basic well logs and thermal maturity data.

References

- Ambrose, R.J., Hartman, R.C., Diaz-Campos, M., Akkutlu, I.Y., Sondergeld, C.H. 2012. Shale Gas-in-Place Calculations Part I: New Pore-Scale Considerations. SPE Journal. March. p. 219-229.
- Beaumont, C., Quinlan, G.M., Hamilton, J. 1987. The Alleghanian Orogeny and Its Relationship to the Evolution of the Eastern Interior, North America. Sedimentary basins and Basin-Forming Mechanisms. Canadian Society of Petroleum Geologists, Memoir 12, p. 425-445.
- Blakey, R. 2013. Middle Devonian (385 ma). Paleogeography and Geologic Evolution of North America. <http://cpgeosystems.com/nam.html>
- Chareonsuppanimit, P., Mohammad, S.A., Robinson Jr., R.L., Gasem, A.M. 2012. High-pressure adsorption of gases on shales: Measurement and modeling. International Journal of Coal Geology 95. p. 34-46.
- DeCelles, P. G., Giles, K. A. 1996. Foreland basin systems. Basin Research. 8. p. 105–123.
- Emery, M., Zagorski, W. A. 2013. Integration of Rock and Petrophysical Data to Determine Key Reservoir Properties for the Marcellus Shale in the Gulla No. 3H Pilot Hole in Washington County, Pennsylvania. Black Shale Core Workshop. AAPG Pre-Convention Short Course #9.
- Fail, R.T. 1999. Part IV. Geologic History, Chapter 33: Paleozoic. The Geology of Pennsylvania. PA DCNR. p. 419-434.
- Gasparik, M., Bertier, P., Gensterblum, Y., Ghanizadeh, A., Krooss, B.M., Littke, R. 2014. Geological controls on the methane storage capacity in organic-rich shales. International Journal of Coal Geology 123. p. 34-51.
- Guo, S. 2013. Experimental study on isothermal adsorption of methane gas on three shale samples from Upper Paleozoic strata of the Ordos Basin. Journal of Petroleum Science and Engineering 110. p. 132-138.
- Harrison, W.E. 1979. Levels of Graphitization of Kerogen as a Potentially Useful Method of Assessing Paleotemperatures. SEPM Special Publication No. 26, March. p. 45-53.
- Hart, B.S., Steen, A.S. 2015. Programmed Pyrolysis (Rock-Eval) data and shale paleoenvironmental analysis: A review. Interpretation, Vol. 3, No.1. February. p. SH41-SH58.
- Hartman, C. 2012. Weatherford Laboratories Sorption Isotherm Technology Summary.
- Heller, R., Zoback, M. 2014. Adsorption of methane and carbon dioxide on gas shale and pure mineral samples. Journal of Unconventional Oil and Gas Resources 8. p. 14-24.
- Horsfield, B., Rullkötter, J. 1994. Diagenesis, Catagenesis, and Metagenesis of Organic Matter. The petroleum system – from source to trap: AAPG Memoir 60. Chapter 10. p. 189-199.
- Jarvie, D. M., 1991. Total Organic Carbon (TOC) Analysis. Source and Migration Processes and Evaluation Techniques. Chapter 11, 113-118.
- Kethireddy, N., Chen, H., Heidari, Z. 2014. Quantifying the Effect of Kerogen on Resistivity Measurements in organic-Rich Mudrocks. Petrophysics, Vol. 55, No. 2 April. p. 136-146.

- Kinghorn, R.R.F., Rahman, M. 1983. Specific gravity as a kerogen type and maturity indicator with special reference to amorphous kerogens. *Journal of Petroleum Geology*, 6, 2. p. 179-194.
- Kulander, C., Ryder, R., 2005, Regional seismic lines across the Rome Trough and Allegheny Plateau of northern West Virginia, western Maryland, and southwestern Pennsylvania: USGS.
- Kwiecińska, B., Petersen, H.I. 2004. Graphite, semi-graphite, natural coke, and natural char classification – ICCP system. *International Journal of Coal Geology* 57. p. 99-116.
- Langmuir, I. 1918. The Adsorption of Gases on Plane Surfaces of Glass, Mica, and Platinum. *Journal of American Chemistry Society*. 40 (9), 1361-1403.
- Lash, G. G., Engelder, T. 2009. The Middle Devonian Marcellus Shale – a Record of Eustasy and Basin Dynamics. *AAPG Search and Discovery Article #30104*.
- Laughrey, C.D., Ruble, T.E., Lemmens, H., Kostelnik, J., Butcher, A.R., Walker, G., Knowles, W. 2011. Black Shale Diagenesis: Insights from Integrated High-Definition Analyses of Post-Mature Marcellus Formation Rocks, Northeastern Pennsylvania. *Search and Discovery Article #110150*
- Lu, X-C., Li, F-C., Watson, T.A. 1995. Adsorption measurements in Devonian shales. *Fuel*, Volume 74, Number 4. p. 599-603.
- Mason, B., Berry, L.G. 1968. Determinative Mineralogy. *Elements of Mineralogy*. W. H. Freeman and Company. p. 167-194.
- Nordeng, S.H. 2012. Basic Geochemical Evaluation of Unconventional Resource Plays. *NDGS Newsletter*; January, Vol. 39 Issue 1, p. 14.
- Olusanmi, E. O., Sonnenberg, S. A. 2013. Geologic Characterization and the Depositional Environment of the Middle Devonian Marcellus Shale, Appalachian Basin, NE USA. *URTeC #1563700*
- Park, H., Barbeau Jr., D. L., Rickenbaker, A., Bachmann-Krug, D., Gehrels, G. 2010. Application of Foreland Basin Detrital-Zircon Geochronology to the Reconstruction of the Southern and central Appalachian Orogeny: *The Journal of Geology*, 118. p. 23-44
- Peters, K.E. 1986. Guidelines for Evaluating petroleum Source Rock Using Programmed Pyrolysis. *The American Association of Petroleum Geologists Bulletin*. V.70, No. 3 March. p. 318-329.
- Petersen, H. I., Schovsbo, N. H., Nielsen, A. T. 2013. Reflectance measurements of zooclasts and solid bitumen in Lower Paleozoic shales, southern Scandinavia: Correlation to vitrinite reflectance. *International Journal of Coal Geology*. 114. p. 1-18.
- Repetski, J. E., Ryder, R. T., Harper, J. A., Trippi, M. H. 2002, Thermal maturity patterns (CAI and % Ro) in the Ordovician and Devonian rocks of the Appalachian Basin in Pennsylvania: U.S. Geological Survey Open-File Report 02-302.
- Ross, D.J.K., Bustin, R.M. 2009. The importance of shale composition and pore structure upon gas storage potential of shale gas reservoirs. *Marine and Petroleum Geology* 26. p. 916-927.

- Ruppert, L.F., Ryder, R.T. 2014. Coal and petroleum resources in the Appalachian basin; Distribution, Geologic Framework, and Geochemical character: U.S. Geological Survey Professional Paper 1708–A.1 through I.1, <http://dx.doi.org/10.3133/pp1708>.
- Senftle, J. T., Landis, C. R. 1991. Vitrinite Reflectance as a tool to Asses Thermal Maturity. Source and Migration Process and evaluation Techniques. p. 119-125.
- Schettler Jr., P.D., Parmely, C.R., Juniata C. 1991. Contributions to Total Storage Capacity in Devonian Shales. SPE 23422. P. 77-88
- Schieber, J. 2013. SEM Observaions on Ion-milled Samples of Devonian Black Shales from Indiana and New York: The Petrographic Context of Multiple Pore Types. Electron microscopy of shale hydrocarbon reservoirs: AAPG Memoir 102, p. 153-171.
- U.S. Energy Information Administration, Drilling Productivity Report. <http://www.eia.gov/petroleum/drilling/>, September 14, 2015.
- Unconventional Wells through March 31, 2015. Marcellus Center for Outreach and Research. 7/8/2015
- Wendt, A.K., Arthur, M.A., Slingerland, R. Kohl, D., Bracht, R., Engelder, T. 2015. Geochemistry and depositional history of the Union Springs Member, Marcellus Formation in central Pennsylvania. Interpretation, Vol.3, No. 3 August. p. SV17-SV33, 11 FIGS.
- Zagorski, W.A., Bowman, D.C., Emery, M., Wrightstone, G.R. 2001. An overview of Some Key Factors Controlling Well Productivity in Core Areas of the Appalachian Basin Marcellus Shale Play. Search and Discovery Article #110147. June 13.
- Zagorski, W. A., Wrightstone, G. R., Bowman, D. C. 2012, The Appalachian Basin Marcellus gas play: Its history of development, geologic controls on production, and future potential as a world-class reservoir. Shale reservoirs—Giant resources for the 21st century: AAPG Memoir 97, p. 172 – 200.
- Zhang, T., Ellis, G.S., Ruppel, S.C., Milliken, K., Yang, R. 2012. Effect of organic-matter type and thermal maturity on methane adsorption in shale-gas systems. Organic Geochemistry 47. p. 120-131.

Biographical Information

Alexander Miller is currently an exploration geologist in the oil and gas industry. He holds a B.A. in Geology (2012) from the University of Colorado and a M.S. in Geology (2015) from the University of Texas at Arlington. Outside of his interests in the geological sciences, Alexander enjoys golfing and snowboarding.